DISEASES AND DISORDERS

TNIK is a conserved regulator of glucose and lipid metabolism in obesity

T. C. Phung Pham[1,2], Lucile Dollet[3], Mona S. Ali[1,2], Steffen H. Raun[1,2], Lisbeth L. V. Møller[1,2], Abbas Jafari[4], Nicholas Ditzel[5,6], Nicoline R. Andersen[1], Andreas M. Fritzen[1], Zachary Gerhart-Hines[3], Bente Kiens[1], Anu Suomalainen[7,8], Stephen J. Simpson[9,10], Morten Salling Olsen[11,12], Arnd Kieser[13,14], Peter Schjerling[15,16], Anni I. Nieminen[17], Erik A. Richter[1], Essi Havula[7]*, Lykke Sylow[1,2]*

Obesity and type 2 diabetes (T2D) are growing health challenges with unmet treatment needs. Traf2- and NCK-interacting protein kinase (TNIK) is a recently identified obesity- and T2D-associated gene with unknown functions. We show that TNIK governs lipid and glucose homeostasis in *Drosophila* and mice. Loss of the *Drosophila* ortholog of *TNIK*, *misshapen*, altered the metabolite profiles and impaired de novo lipogenesis in high sugar–fed larvae. *Tnik* knockout mice exhibited hyperlocomotor activity and were protected against diet-induced fat expansion, insulin resistance, and hepatic steatosis. The improved lipid profile of *Tnik* knockout mice was accompanied by enhanced skeletal muscle and adipose tissue insulin-stimulated glucose uptake and glucose and lipid handling. Using the T2D Knowledge Portal and the UK Biobank, we observed associations of *TNIK* variants with blood glucose, HbA1c, body mass index, body fat percentage, and feeding behavior. These results define an untapped paradigm of TNIK-controlled glucose and lipid metabolism.

INTRODUCTION

Obesity is a major health challenge, reaching epidemic proportions with estimated 1.12 billion individuals in 2030 worldwide (*1*). Substantiating its clinical and public health burden, obesity strongly correlates with an increased risk of type 2 diabetes (T2D), cardiovascular diseases, cancer, and mortality (*2*, *3*). Both obesity and T2D are associated with metabolic dysregulation, fat expansion, peripheral insulin resistance, and hepatic steatosis. Understanding the molecular pathways governing glucose and lipid metabolism in molecular detail is essential for identifying potential targets for effective treatment of obesity and T2D.

In recent years, genome-wide association studies (GWAS) have identified many variants associated with obesity and its risk factors (*4*, *5*). Combining GWAS to functional in vivo studies is a crucial step toward understanding relationships between genotypes and phenotypes. However, this approach has only been applied to a few obesity-associated GWAS loci so far (*4*, *6*). Our recent study took such an approach and identified the fly ortholog of Traf2- and NCK-interacting protein kinase (TNIK), *misshapen* (*msn*), as a regulator of dietary sugar tolerance and metabolism in *Drosophila* (*7*), yet the role of TNIK in the pathophysiology of obesity and T2D is unknown.

TNIK has been implicated in various cellular signaling processes, including the activation of c-Jun N terminal kinase (JNK) (*8*) and nuclear factor κB signaling in hematopoietic cells (*8*), and Wnt signaling in colorectal cancer cells (*9*). TNIK is suggested to be regulated by the adenosine 5′-monophosphate (AMP)–activated protein kinase (AMPK) in skeletal muscle in response to exercise in humans (*10*). AMPK and its downstream effectors have been longstanding targets for the development of potential therapeutic strategies that could improve insulin sensitivity (*11*). Together, JNK, nuclear factor κB, Wnt, and AMPK signaling have been implicated in the regulation of glucose and lipid metabolism (*12*–*15*). However, the potential direct role(s) for TNIK and associated signaling pathways in the metabolic control and pathophysiology of obesity and T2D has remained unexplored.

To address this, we integrated obesity models of *Drosophila melanogaster* and mice, metabolomics studies, and a multitude of metabolic screening approaches to investigate the role of TNIK in obesity and metabolic dysfunction. Our study demonstrates a critical role for TNIK/msn in the regulation of energy balance, glucose and fatty acid metabolism, lipid deposition, and insulin sensitivity, both in flies and mice. Together, we show that TNIK could be a potential therapeutic target for enhancing glucose tolerance and

[1]Department of Nutrition, Exercise and Sports, Faculty of Science, University of Copenhagen, Copenhagen, Denmark. [2]Department of Biomedical Sciences, Faculty of Health and Medical Sciences, University of Copenhagen, Copenhagen, Denmark. [3]Novo Nordisk Foundation Center for Basic Metabolic Research, Faculty of Health and Medical Sciences, University of Copenhagen, Copenhagen, Denmark. [4]Department of Cellular and Molecular Medicine, University of Copenhagen, Copenhagen, Denmark. [5]Molecular Endocrinology and Stem Cell Research Unit (KMEB), Department of Endocrinology and Metabolism, Odense University Hospital and University of Southern Denmark, Odense, Denmark. [6]Biomedical Laboratory, The Faculty of Health Sciences, University of Southern Denmark, Denmark. [7]Stem Cells and Metabolism Research Program, Faculty of Medicine, University of Helsinki, Finland. [8]Helsinki University Hospital, HUS Diagnostic Center, Helsinki 00290, Finland. [9]Charles Perkins Centre, The University of Sydney, Camperdown 2006, Australia. [10]School of Life and Environmental Sciences, The University of Sydney, Camperdown, 2006, Australia. [11]Laboratory for Molecular Cardiology, Department of Cardiology, Copenhagen University Hospital, Rigshospitalet, Building 9312, Henrik Harpestrengs Vej 4C, Copenhagen 2100, Denmark. [12]Laboratory for Molecular Cardiology, Department of Biomedical Sciences, University of Copenhagen, Copenhagen, Denmark. [13]Helmholtz Centre Munich–German Research Centre for Environmental Health, Research Unit Signaling and Translation, Ingolstaedter Landstr. 1, Neuherberg 85764, Germany. [14]German Center for Infection Research (DZIF), Partner Site Munich, Munich, Germany. [15]Institute of Sports Medicine, Department of Orthopaedic Surgery M, Bispebjerg Hospital, Copenhagen, Denmark. [16]Center for Healthy Aging, Faculty of Health and Medical Sciences, University of Copenhagen, Copenhagen, Denmark. [17]FIMM Metabolomics Unit, Institute for Molecular Medicine Finland, University of Helsinki, Finland.
*Corresponding author. Email: essi.havula@helsinki.fi (E.H.); lykkesylow@sund.ku.dk (L.S.)

insulin sensitivity in obesity and obesity-related comorbidities, including T2D.

RESULTS

The TNIK *Drosophila* ortholog *msn* regulates sugar-induced metabolism

The TNIK fly ortholog, MAP4K family kinase *msn* was recently identified as a regulator of dietary sugar tolerance and metabolism in *Drosophila* (*7*). To study the function of *TNIK*/*msn* in detail, we followed larval development of RNA interference (RNAi)–mediated whole-body knockdown (KD) *msn* flies and found that the development of *msn* flies fed a high-sugar diet (HSD) was markedly delayed (Fig. 1, A and B). The loss of *msn* on both high-protein diet (HPD) and HSD resulted in almost complete pupal lethality as measured by eclosion rate (Fig. 1B). On HSD, the *msn* RNAi larvae were severely hyperglycemic, while the circulating glucose levels in hemolymph of *msn* RNAi larvae on HPD were comparable to controls (Fig. 1C). Together, these results show that loss of *msn* compromises whole-body sugar homeostasis under high-sugar conditions.

Having established TNIK/msn as a critical regulator of sugar-induced metabolism in vivo, we next sought to determine the underlying molecular mechanisms by which short-term sugar feeding affects the whole-body metabolism of *msn* RNAi larvae. To this end, freshly hatched first instar larvae were first kept on HPD for 48 hours, after which they were transferred to either HPD or HSD for 16 hours (Fig. 1D). The principal components plot derived from targeted metabolomics of whole larvae revealed a notable difference in the whole-body metabolites between control and *msn* RNAi larvae in response to HSD feeding (Fig. 1E and fig. S1A).

In control larvae, transient sugar feeding elevated the levels of the glycolytic metabolites lactic acid and pyruvic acid; fatty acid metabolite lauric acid; and purine metabolites inosine, xanthine, and hypoxanthine, while pyrimidine metabolites uridine monophosphate (UMP), uridine diphosphate (UDP), and UDP-glucose, the precursor of glycogen, decreased [Fig. 1F and data S1 (ctrl HPD versus HSD metabolites)]. In *msn* RNAi larvae, the metabolic response to HSD was notably different and characterized by decreased levels of several fatty acid metabolites, including oleate, palmitoleic acid, linoleate, and gamma-linolenic acid [Fig. 1F and data S2 (msn HPD versus HSD metabolites)]. In addition, low levels of tyrosine metabolites hydroxyphenylpyruvate, hydroxyphenyl lactate, and homogentisate, as well as essential amino acid lysine, which is a precursor of carnitine biosynthetic pathway together with trimethyllysine, were present in *msn* RNAi larvae in response to sugar feeding (Fig. 1F).

A four-way plot, comparing $\log_2$ fold metabolic changes for each group, revealed the metabolites that were affected by both the diet and the genotype (Fig. 1, G and H, and fig. S1B). The top metabolites that were increased by sugar in an *msn*-dependent manner included (i) tyrosine metabolite homogentisate; (ii) the glycolytic and tricarboxylic acid cycle metabolites lactate, pyruvate, citramalate, and itaconate; (ii) purine metabolites xanthine and hypoxanthine; (iii) fatty acid metabolite malonate; and (iv) γ-aminobutyric acid (Fig. 1H). The top metabolite that was decreased by sugar in an *msn*-dependent manner was dihydroxyacetone phosphate (DHAP; Fig. 1G and fig. S1B). In addition to being a glycolytic metabolite, DHAP is the first step of the glycerol-3-phosphate synthesis. Situated at the metabolic junction between glycolysis and lipid synthesis (*16*) and being an activator of the mechanistic target of rapamycin complex 1 (mTORC1), TNIK could, via DHAP, be implicated in the ability of mTORC1 to sense glucose availability in the cell. The following top metabolites, decreased by sugar in an *msn*-dependent manner, were oxidized glutathione, phosphocholine, the precursor of major membrane component phosphatidylcholine, pyrimidine metabolites UDP and UMP, the glycogen precursor UDP-glucose, methyl donor betaine (trimethylglycine), and the end-product of pentose phosphate pathway ribose 5-phosphate (Fig. 1G and fig. S1B).

Reduced levels of glycolytic and fatty acid metabolites in *msn* RNAi larvae prompted us to measure the sugar-induced expression of the de novo lipogenic genes fatty acid synthase (*FAS*) and acetyl–coenzyme A–carboxylase (*ACC*) in response to sugar feeding. In line with the metabolomics results, the sugar-induced expression of both *FAS* and *ACC* was blunted in *msn* RNAi larvae (Fig. 1I), suggesting that *msn* is required for de novo lipogenesis in high-sugar conditions. Together, loss of *msn* in *Drosophila* leads to widespread changes in the metabolome, including down-regulation of several anabolic pathways such as de novo lipogenesis and glycogen synthesis, and one-carbon metabolism–dependent nucleotide, glutathione, and phospholipid homeostasis.

Global loss of TNIK protects against diet-induced obesity in mice

To corroborate our discoveries in *Drosophila* in a vertebrate model organism, we next sought to mechanistically determine the role of TNIK in metabolic disease using whole-body *Tnik* knockout (KO) mice (*17*). *Tnik* KO mice revealed a leaner phenotype in comparison to wild-type (WT) control littermates (fig. S2A). This was due to lower total fat and lean mass in both sexes (fig. S2, B and C).

Measuring TNIK protein expression across a diverse array of tissues in WT mice revealed the highest protein content of TNIK in the brain, skeletal muscle, heart, and spleen (Fig. 2A). Notably, TNIK protein was not detectable in adipose tissue, including brown, gonadal, and subcutaneous adipose tissue (Fig. 2A), contrasting earlier reports that TNIK is ubiquitously expressed on a transcript level (*18*).

High-throughput targeted plasma metabolomics analysis revealed down-regulation in circulating lactate and pyruvate levels and up-regulation of several fatty acids, including gamma-linolenic acid [C18:3 (n-6)], docosahexaenoic acid [C22:6 (n-3)], oleate [C18:1 (n-9)], and myristic acid (C14:0) [fig. S3 and data S3 (WT versus *Tnik* KO plasma metabolomics)]. The lean phenotype in conjunction with elevated fatty acid levels suggests that global loss of TNIK leads to alterations in whole-body lipid flux and adipose tissue deposition.

To investigate the potential role of TNIK in metabolic disease, we fed WT and *Tnik* KO mice of both sexes a high-fat high-sucrose (HFHS) diet (45% calories from fat; drinking water enriched with 10% sucrose ad libitum) and chow diet (chow diet; regular water ad libitum) (Fig. 2B, CHOW). Despite having the largest caloric intake of all four study groups (Fig. 2C; caloric intake from food and sucrose shown separately in fig. S2D), the body weight (BW) gain of HFHS-fed *Tnik* KO female mice was attenuated (Fig. 2D). Magnetic resonance imaging scans revealed that the *Tnik* KO female mice were protected from diet-induced fat expansion (Fig. 2E), whereas lean mass was comparable among all groups (Fig. 2F). For male mice, we made similar observations on

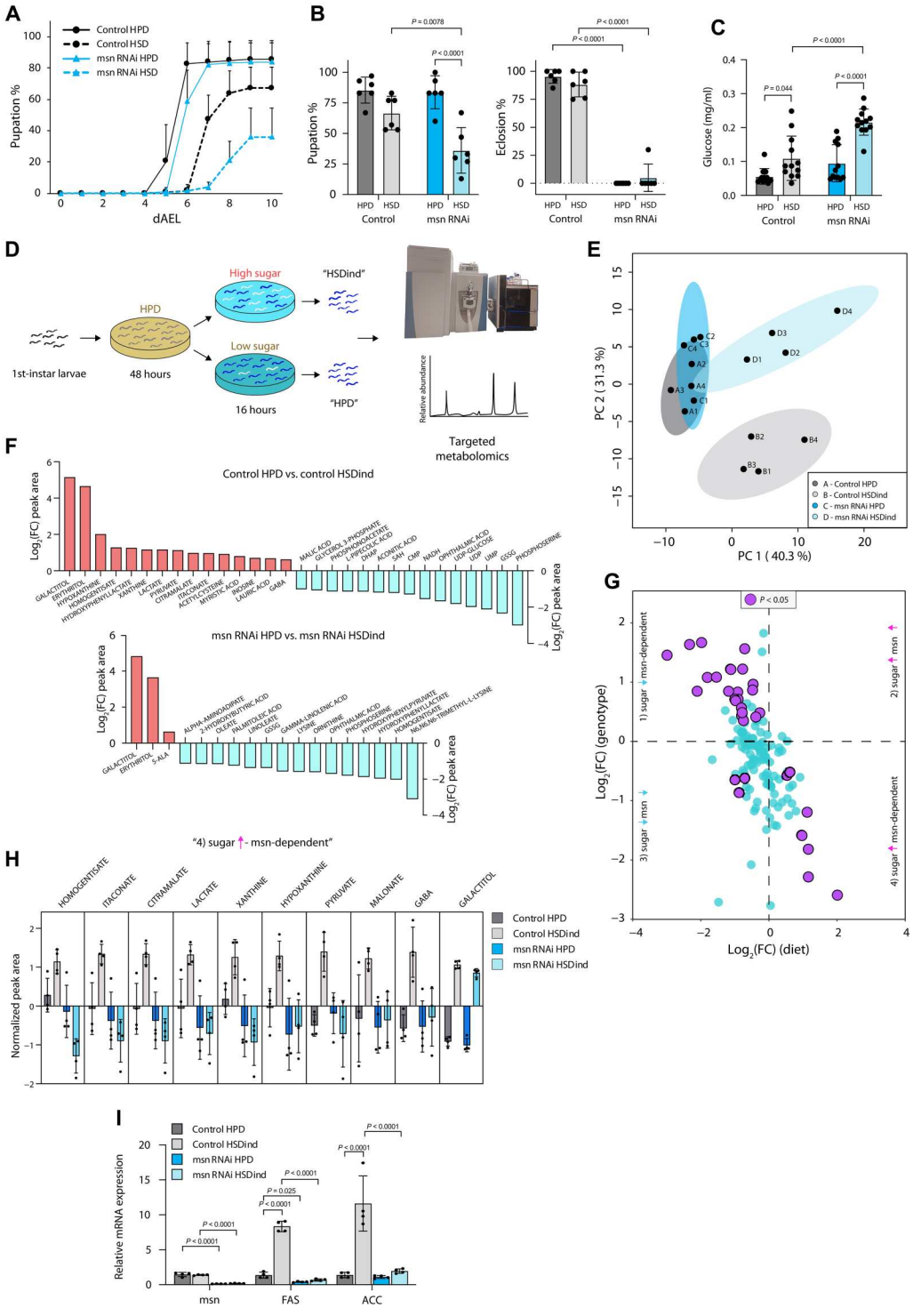

Fig. 1. *Drosophila misshapen* regulates sugar induced metabolism. (**A**) Pupation kinetics in control (*Tub-GAL4*>) and RNA interference (RNAi)–mediated whole-body *misshapen* (*msn*) knockdown fed high-protein diet (HPD) or high-sugar diet (HSD) . (**B**) Total pupation and eclosion of *msn* RNAi and control animals on HPD and HSD. $n = 6$ vials (each with 30 larvae) per diet and genotype. dAEL, days after egg laying. (**C**) Circulating glucose levels in hemolymph of *msn* RNAi and control prewandering third-instar larvae raised on HPD or HPD with added sugar. $n = 12$ (each with 10 larvae) per diet and genotype. (**D**) Experimental outline of sugar induction. First-instar larvae were grown on HPD for 48 hours followed by 16 hours of HPD or HSD feeding. The experimental diets were supplemented with blue food dye to monitor feeding and selection of third-instar fed-state animals for metabolomics and RNA extraction. (**E**) Principal components analysis (PCA) of the 16 samples analyzed (four samples per diet and genotype). (**F**) Top 15 up- and down-regulated metabolites ($P < 0.05$) by sugar in control (top plot) and msn RNAi (bottom plot) animals. For *msn* RNAi, there were only three significantly up-regulated metabolites. (**G**) Four-way plot presenting the *msn*-dependent HSD-regulated metabolites [$P<0.05$; logFC (fold change) > 0/logFC <0]. (**H**) Metabolites that were up-regulated by sugar in an *msn*-dependent manner ($P < 0.05$). (**I**) Whole-body expression of *msn*, *FAS*, and *ACC* in control and *msn* RNAi larvae. $n = 4$ (five second-instar larvae per sample) per diet and genotype. Statistical significances were calculated using the two-way analysis of variance (ANOVA) in conjunction with Tukey's multiple comparisons test (B and C) or by one-way ANOVA in conjunction with Dunnett's multiple comparisons test (I). Data are presented as means ± SD (A to C and I). Metabolomics data (E to H) were analyzed in MetaboAnalyst (see Materials and Methods for further information).

caloric intake, weight gain, and fat mass (Fig. 2, H to J and L; caloric intake from food and sucrose shown separately in fig. S2E), although lean mass was 8% reduced in *Tnik* KO mice (Fig. 2K). Representative photographs of the obesity-resistant phenotype for female and male mice are shown in Fig. 2 (G and L). Tibia length as a direct measure for body size shows that there is no difference in size between WT and *Tnik* KO mice (fig. S2Q).

The lean phenotype could, in part, be driven by increased ambulant activity level because a 1.4-fold increase in oxygen consumption (VO_2) accompanied by a sevenfold increase in ambulant activity in the dark period (Fig. 2, M to P) was evident in *Tnik* KO male mice. Chow-fed *Tnik* KO mice exhibited a similar energy balance to WT mice despite comparable energy intake and higher energy expenditure (Fig. 2, Q to S). Plotted individual energy

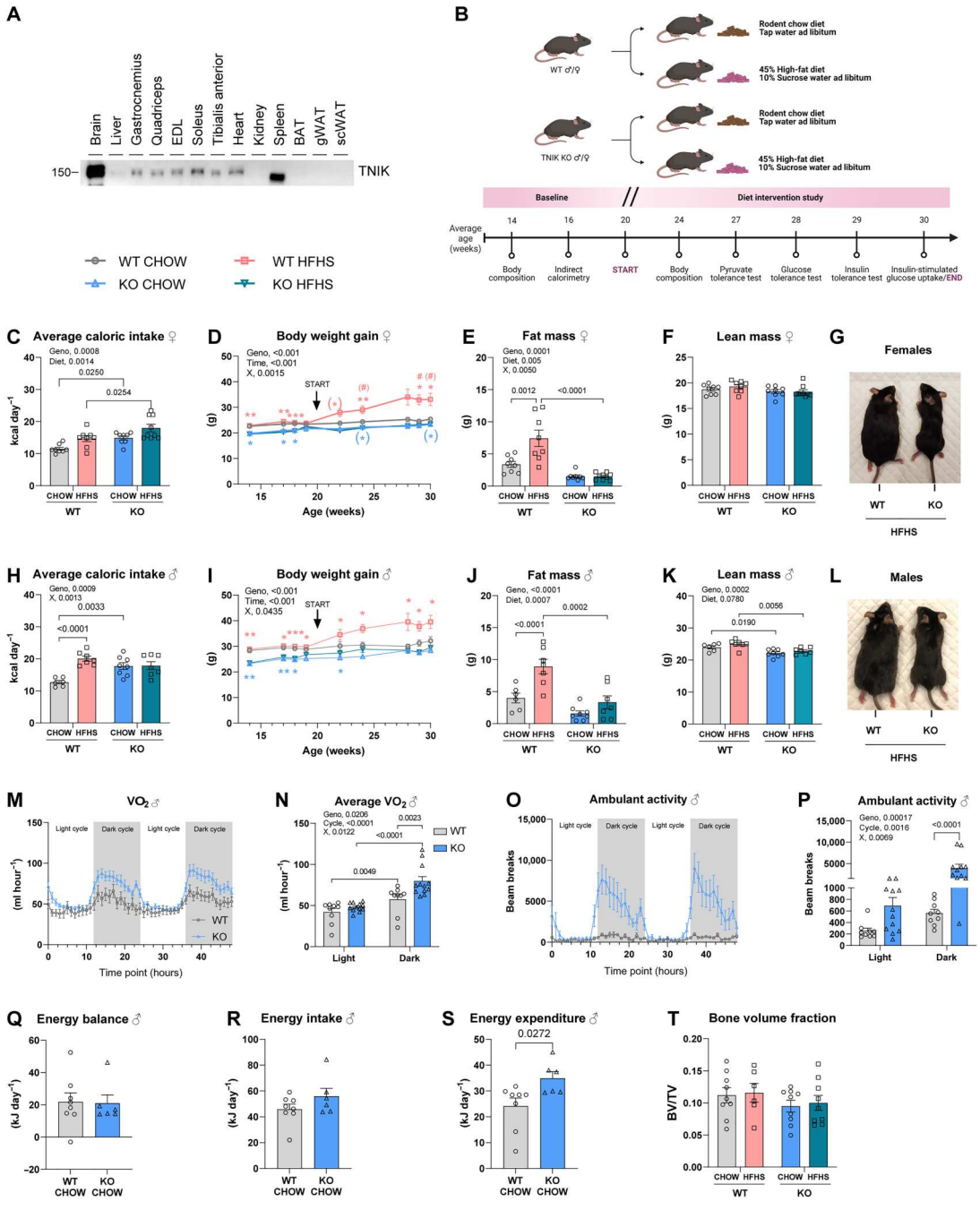

Fig. 2. Loss of TNIK protects against diet-induced obesity in mice. (**A**) TNIK protein content in mouse tissues ($n = 4$, aged 12 weeks). (**B**) Experiments at indicated weeks of age before or during 10 weeks of CHOW/high-fat high-sucrose (HFHS) ad libitum diet. CHOW wildtype (WT) littermate female/male (f/m), $n = 8/6$; HFHS WT f/m, $n = 8/7$; CHOW *Tnik* knockout (KO) f/m, $n = 8/8$; HFHS KO f/m, $n = 9/7$. (**C**) Average caloric intake and (**D**) body weight gain of female mice during 10 week of CHOW/HFHS. Individual *P* values in order of comparisons: genotype effect within CHOW (blue), $^{*}P = 0.0273$, $^{*}P = 0.0147$, $^{*}P = 0.0117$, $(^{*})P = 0.0587$, and $(^{*})P = 0.0989$; genotype effect within HFHS (pink), $^{**}P = 0.0016$, $^{**}P = 0.0015$, $^{***}P = 0.0009$, $(^{*})P = 0.0515$, $^{**}P = 0.0091$, $^{*}P = 0.0116$, and $^{*}P = 0.0325$; and diet effect within WT (pink), $(\#)P = 0.0734$, $\#P = 0.0224$, and $(\#)P = 0.0743$. (**E**) Absolute fat and (**F**) lean mass of female mice at 4 week of CHOW/HFHS. (**G**) Representative image of HFHS-fed female mice. (**H**) Average caloric intake and (**I**) body weight gain of male mice on 10 weeks of CHOW/HFHS. Individual *P* values in order of comparisons: genotype effect within CHOW (blue), $^{**}P = 0.0047$, $^{**}P = 0.0020$, $^{**}P = 0.0011$, $^{*}P = 0.0114$, and $^{*}P = 0.0403$ and genotype effect within HFHS (pink), $^{**}P = 0.0031$, $^{*}P = 0.0122$, $^{**}P = 0.0002$, $^{*}P = 0.0114$, $^{*}P = 0.0102$, $^{*}P = 0.0167$, and $(^{*})P = 0.0507$. (**J**) Absolute fat and (**K**) lean mass of male mice at 4 weeks of CHOW/HFHS. (**L**) Representative image of HFHS-fed male mice. (**M**) Oxygen consumption (VO_2) and (**O**) ambulant activity of CHOW-fed male mice (WT/KO, $n = 9/12$) over 48 hours. (**N**) Average VO_2 and (**P**) ambulant activity during the light/dark cycle. Mean values of (**Q**) energy balance, (**R**) energy intake, and (**S**) energy expenditure of CHOW-fed male mice (WT/KO, $n = 8/6$) over a 2-day period. (**T**) Bone volume fraction of female and male mice. Data are shown as means ± SEM including individual values where applicable. Statistical significance calculated by two-way ANOVA with Šídák's multiple comparisons test (C, E, F, H, J, K, and T), two-way ANOVA RM with Šídák's multiple comparisons test (N and P), mixed-effect analysis with Tukey's multiple comparisons test (D and I), or by unpaired *t* test (Q to S). Geno, main genotype effect; diet, main diet effect; X, interaction between genotype and diet.

expenditure against BW (fig. S2, F and G) demonstrates that the regression lines for WT and *Tnik* KO mice do not significantly differ, indicating that there is no mass-independent group effect. The respiratory exchange ratio was comparable between genotypes (fig. S2, H and I). However, *Tnik* KO mice demonstrated ~45 and ~70% elevated rates of carbohydrate and fatty acid oxidation during the dark cycle, respectively, possibly to facilitate the heightened total energy expenditure (fig. S2, J to M).

To explore whether the *Tnik* KO mice displayed an exercise-trained phenotype due to the increased ambulant nightly activity, we measured running capacity, grip strength, and bone volume fraction that are known to be increased in response to exercise training in mice (*19*–*21*). Despite increased ambulant nightly activity of the mice, running capacity was slightly reduced in the *Tnik* KO mice (fig. S2N). Grip strength, performed horizontally but not vertically, was reduced by diet in both genotypes (fig. S2, O and P). Bone volume fraction [defined as bone volume per total tissue volume (BV/TV)] was similar between WT and *Tnik* KO mice (Fig. 2T). On the basis of the parameters, the increased ambulant nightly activity hence did not confer a trained phenotype. Together, these data show that *Tnik* KO mice display a remarkable obesity-resistant phenotype that confers protection against BW gain and fat expansion independent of sex.

Loss of TNIK protects against diet-induced metabolic dysfunction in mice

In obesity and T2D, the ability to clear glucose from the blood stream decreases as insulin resistance gradually increases. Without compensatory pancreatic insulin secretion to overcome insulin resistance, decreased glucose clearance leads to increased glucose levels in response to a glucose challenge. This situation was recapitulated in the obese WT mice on a HFHS diet, evidenced by upshifted glucose response curve (Fig. 3A) and elevated levels of circulating insulin (Fig. 3B) during a glucose tolerance test. Although not reaching statistical significance, the *Tnik* KO mice exhibited a notable trend of protection against diet-induced glucose intolerance and hyperinsulinemia (Fig. 3, A and B). Calculating the incremental area under the curve (iAUC) of blood glucose showed similarity between groups (Fig. 3C). Notably, negative incremental AUC values were recorded for one chow-fed WT mouse and four HFHS-fed *Tnik* KO mice, as their blood glucose levels dropped below fasting glucose levels during the glucose tolerance test, indicative of an efficient glucose metabolism, likely facilitated by high insulin secretion (Fig. 3B), and increased glucose uptake into peripheral tissues.

In alignment with reduced blood glucose and insulin levels, insulin sensitivity was high in *Tnik* KO mice irrespective of diet, measured during an insulin tolerance test (Fig. 3, D and E). The insulin tolerance test had to be prematurely terminated in 8 of 25 *Tnik* KO mice (6 *Tnik* KO CHOW and 2 *Tnik* KO HFHS) because of hypoglycemia (blood glucose, <1.7 mM), an event that did not occur in any of the WT mice.

These insulin-sensitive *Tnik* KO mice exhibited a flatter glycemic excursion curve during a pyruvate tolerance test, indicating a more efficient conversion of pyruvate to glucose and/or better glucose clearance. The pyruvate tolerance test had to be prematurely terminated in two of seven *Tnik* KO HFHS mice because of hypoglycemia. Thus, *Tnik* KO mice were protected from developing pyruvate intolerance, indicative of hepatic insulin resistance (Fig. 3, F and G).

We have combined sexes for the glucose, insulin, and pyruvate tolerance tests. Sex-specific glycemic excursion curves and related measures obtained for the glucose, insulin, and pyruvate tolerance tests are shown in fig. S4 (A to O). Together, these findings show that loss of TNIK increases insulin sensitivity and effectively protects against diet-induced insulin resistance and glucose intolerance in mice.

Insulin-stimulated skeletal muscle glucose uptake is increased by loss of TNIK

Skeletal muscle is a major tissue in whole-body glucose metabolism, and skeletal muscle insulin resistance contributes to the development of T2D (*22*). We therefore determined 2-deoxy-D-glucose (2DG) clearance into three different muscles [gastrocnemius, tibialis anterior (TA), and soleus] using isotopic tracer combined with in vivo insulin stimulation (Fig. 4, A and B). As expected, in WT mice, HFHS diet reduced insulin-stimulated 2DG clearance across gastrocnemius, TA, and soleus muscles (Fig. 4B). The loss of TNIK resulted in a complete rescue of HFHS-induced insulin resistance as insulin-stimulated 2DG clearance was increased across the analyzed muscles (Fig. 4B). In line with TNIK being a negative regulator of insulin sensitivity, HFHS diet increased TNIK expression in TA of WT mice; however, this effect was not seen in gastrocnemius (fig. S5J).

To gain mechanistic insights underlying the enhanced skeletal muscle 2DG clearance in *Tnik* KO mice fed either CHOW or HFHS diet, we next investigated proteins involved in glucose and lipid handling and insulin signaling in gastrocnemius muscle (schematically illustrated in Fig. 4C). Protein content of the glucose-handling proteins hexokinase II (HKII) and glycogen synthase (GS) were elevated, while glucose transporter type 4 (GLUT4) content was unchanged by *Tnik* KO (Fig. 4D). Despite GS protein up-regulation by 24%, glycogen content tended to be down-regulated in *Tnik* KO mice (Fig. 4, D and E).

Corroborating our metabolomics findings that loss of TNIK induced a marked metabolic shift, the skeletal muscle protein content of pyruvate dehydrogenase (PDH) E1α, the convergence point for glycolysis and mitochondrial adenosine 5′-triphosphate (ATP) synthesis, and the fatty acid transporter protein cluster of differentiation (CD36) were up-regulated in *Tnik* KO mice (Fig. 4, D and H).

Canonical insulin signaling was markedly elevated in skeletal muscle of *Tnik* KO mice, evident by increased insulin-stimulated phosphorylation of Akt S473, Akt T308, TBC1D4 T642, FoxO1 S256, and GSK3β S9 (Fig. 4, F and H). The augmentation in the ratio of phosphorylated protein to total protein is sustained for TBC1D4 but not for Akt2 (fig. S5I).

We next asked whether the insulin-sensitizing effect of *Tnik* KO was due to direct TNIK effects on muscle. To that end, we measured insulin signaling in small interfering RNA (siRNA)–mediated *Tnik* knockdown (KD) (63%; fig. S5A) C2C12 myotubes.

Tnik KD did not alter insulin-stimulated phosphorylation of Akt at T308 and S473 and TBC1D4 at T642 (fig. S5, B, C, and E) or total levels of Akt and TBC1D4 (fig. S5, D and F). In addition, total levels of CD36 were comparable between groups (fig. S5, E and F).

The known TNIK target JNK (*8*) did not seem to be implicated in TNIK's effect on insulin signaling, as insulin-stimulated p-JNK

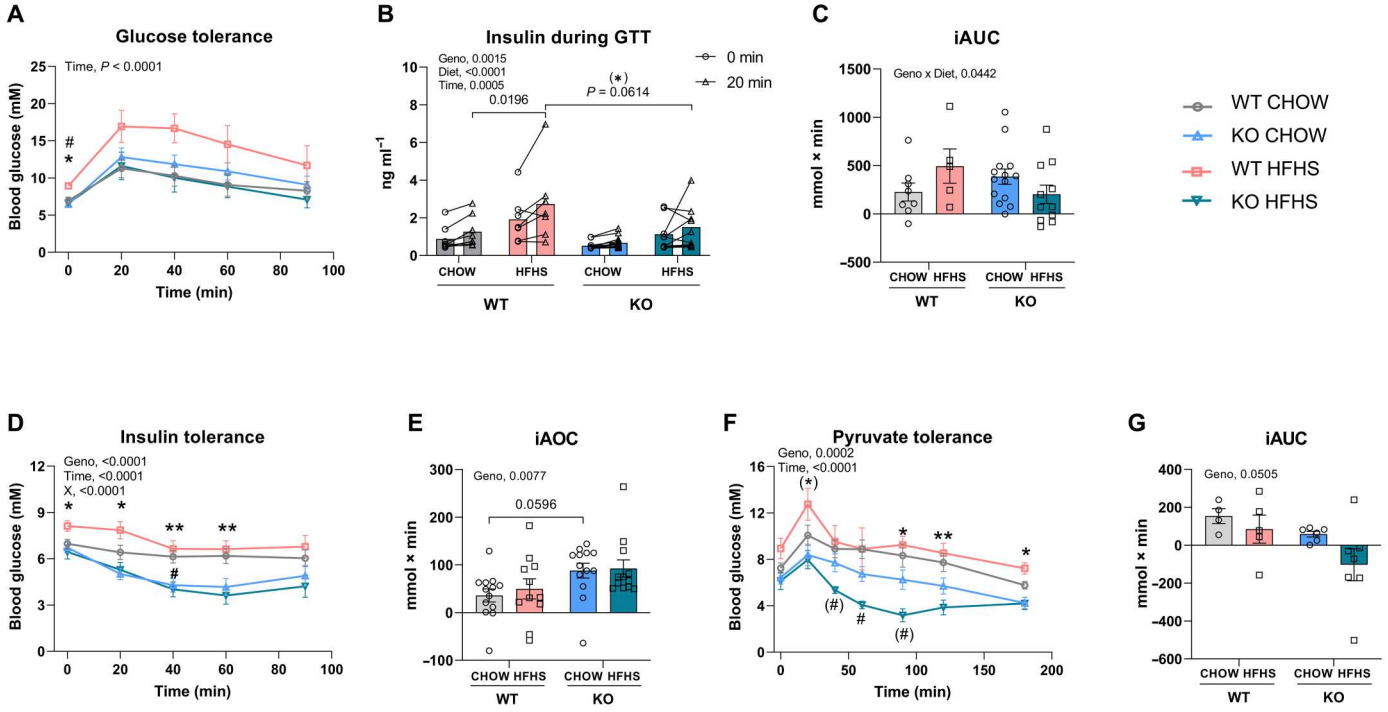

Fig. 3. Loss of TNIK protects against diet-induced metabolic dysfunction in mice. (**A**) Glucose tolerance of female and male mice at 8 weeks of CHOW/high-fat high sucrose (HFHS). CHOW wildtype (WT) f/m, n = 4/4; HFHS WT f/m, n = 3/3; CHOW *Tnik* knockout (KO) f/m, n = 6/8; HFHS KO f/m, n = 7/4. Individual P values in order of comparisons: genotype effect within HFHS diet, *P = 0.0225; diet effect within WT genotype, #P = 0.0444. (**B**) Insulin response before (0 min) and following (20 min) the oral glucose challenge. (**C**) iAUC of glycemic excursion in response to bolus of glucose [2 g kg^{-1} body weight (BW)]. (**D**) Insulin tolerance of female and male mice at 9 weeks of CHOW/HFHS. CHOW WT f/m, n = 7/6; HFHS WT f/m, n = 6/5; CHOW KO f/m, n = 8/5; HFHS KO f/m, n = 8/4. Individual P values in order of comparisons: genotype effect within HFHS diet, *P = 0.0398, *P = 0.0117, **P = 0.0068, and **P = 0.0056 and diet effect within KO genotype, #P = 0.0304 (**E**) Incremental area over the curve (iAOC) of glycemic excursion in response to a bolus of insulin at 0.3 IU kg^{-1} BW. (**F**) Pyruvate tolerance of female and male mice at 7 weeks of CHOW/HFHS. CHOW WT f/m, n = 2/2; HFHS WT f/m, n = 2/3; CHOW KO f/m, n = 2/4; HFHS KO f/m, n = 3/4. Individual P values in order of comparisons: genotype effect within HFHS diet, (*)P = 0.0811, *P = 0.0117, ***P = 0.0009, **P = 0.0098, and *P = 0.0131 and diet effect within KO genotype, (#)P = 0.0965, #P = 0.0284, and (#)P = 0.0547. Data are shown as means + SEM, including individual values where applicable. Statistical significances were calculated using two-way ANOVA RM in conjunction with Tukey's multiple comparisons test (A) or Šídák's multiple comparisons test (C, E, and G) or by mixed-effect analysis in conjunction with Tukey's multiple comparisons test (B, D, and F). Time, main effect of time.

T183/Y185 was unaffected by diet and genotype. Nevertheless, the elevated protein content and activation of both Akt2 and TBC1D4 in *Tnik* KO muscle (Fig. 4, F and H) likely provide a signal for enhanced glucose uptake. Together, these findings reveal a previously uncharacterized role for TNIK in skeletal muscle insulin signaling via Akt and TBC1D4 in vivo, which is not recapitulated C2C12 myotubes in vitro, thus likely driven by organismal effects of *Tnik* KO.

The energy demands of the cells are met by oxidative phosphorylation (OxPhos), a vital process that is carried out by the respiratory chain complexes and ATP synthase in the mitochondria. Following our observations that *Tnik* KO mice exhibited increased energy expenditure and ambulant activity during the dark period, we measured OxPhos protein abundance in gastrocnemius. We observed elevated levels of OxPhos subunits SDHB (complex II), UQCRC2 (complex III), and ATP5A (complex V) (Fig. 4, G and H), indicative of increased oxidative capacity of TNIK-deficient skeletal muscle.

These results reveal intriguing previously undiscovered roles for TNIK on whole-body metabolic regulation via a marked up-regulation of key glucose- and lipid-handling proteins, enhancement of intramyocellular insulin signaling, and likely mitochondrial function in skeletal muscle. These observations are unlikely to be driven by direct effects of skeletal muscle TNIK and points towards the effect on insulin sensitivity being due to systemic effects of *Tnik* KO in nonmuscle tissues.

WAT insulin action is enhanced, and lipid uptake is suppressed in *Tnik* KO mice

Obesity leads to glucose intolerance and insulin resistance in various organs, including white adipose tissue (WAT). Despite only accounting for 5% of glucose uptake following a meal, WAT is important for whole-body glycemic control by secreting hormones and factors that modulate skeletal muscle and liver metabolism (*22*–*24*). Given the observed lean phenotype of the *Tnik* KO mice, we speculated whether the WAT displayed altered insulin action in *Tnik* KO mice. We investigated gonadal WAT (gWAT) and determined insulin sensitivity and insulin signaling following insulin injection in conjunction with isotopic tracer. Insulin-stimulated 2DG clearance was increased in gWAT of HFHS-fed *Tnik* KO mice (Fig. 5A). *Tnik* KO mice were completely protected from gWAT insulin resistance in response to HFHS feeding. Consistent with elevated insulin sensitivity, insulin-stimulated phosphorylation of Akt at S473 and T308 and FoxO1 at S256 was up-regulated in gWAT of *Tnik* KO miceT (Fig. 5, B and C). Phosphorylation of

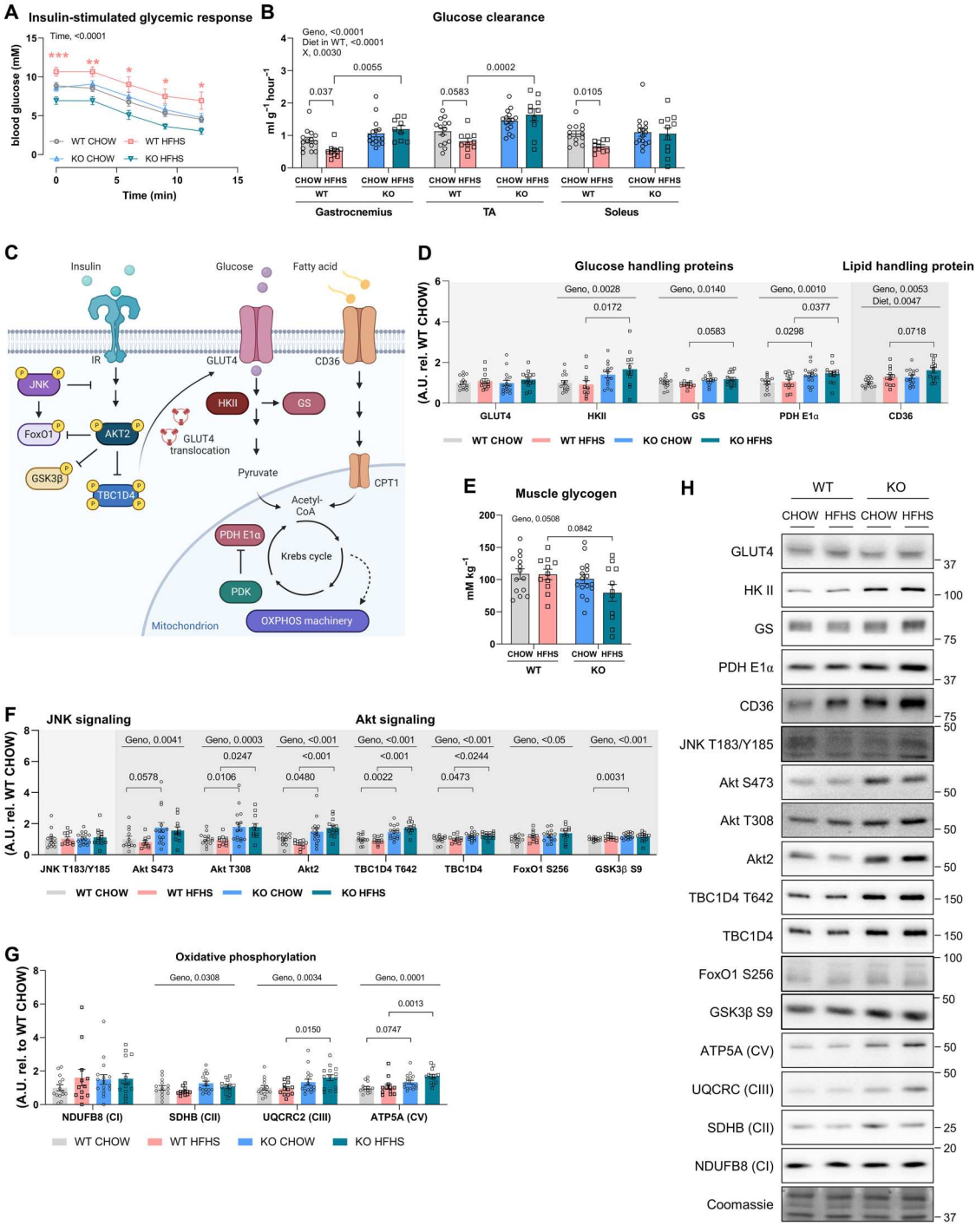

Fig. 4. TNIK deficiency elevates insulin-stimulated glucose uptake into skeletal muscles by increasing canonical Akt signaling, glucose, and lipid handling. (**A**) Glycemic response of female and male chow- or high-fat high-sucrose (HFHS)-fed wildtype (WT) or *Tnik* knockout (KO) mice at 10 weeks of the diet intervention in response to retro-orbital injection of insulin at 0.3 IU kg^{-1} body weight (BW). Individual significant *P* values are provided as the same order of comparisons (left to right): effect of genotype within HFHS diet, ***P = 0.0005, **P = 0.0012, *P = 0.0169, *P = 0.0121, and *P = 0.0289. (**B**) The effect of *Tnik* KO and chow or HFHS diet on insulin-stimulated 2DG clearance in gastrocnemius, TA, and soleus. (**C**) Schematic illustration of pathways analyzed via immunoblotting in gastrocnemius. (**D**) Immunoblot analyses in gastrocnemius of female and male chow- or HFHS-fed WT or *Tnik* KO mice during insulin stimulation: glucose-handling proteins (GLUT4, HKII, GS, and PDH E1α) and lipid-handling proteins (CD36). (**E**) Gastrocnemius muscle glycogen content in female and male *Tnik* KO or WT mice. Immunoblot analyses in gastrocnemius of female and male chow- or HFHS-fed WT or *Tnik* KO mice during insulin stimulation: (**F**) JNK signaling (JNK T183/Y185) and Akt signaling (Akt S473, Akt T308, Akt2, TBC1D4 T642, TBC1D4, FoxO1 S256, and GSK3β S9), (**G**) OxPhos proteins [NDUFB8 (CI), SDHB (CII), UQCRC2 (CIII), and ATP5A (CV)], and (**H**) representative blots. Data are shown as means + SEM, including individual values where applicable. Statistical significances were calculated using mixed-effect analysis in conjunction with Tukey's multiple comparisons test (A) or the two-way ANOVA in conjunction with Tukey's multiple comparisons test (B) or Šídák's multiple comparisons test (C and E to G). A.U., arbitrary units.

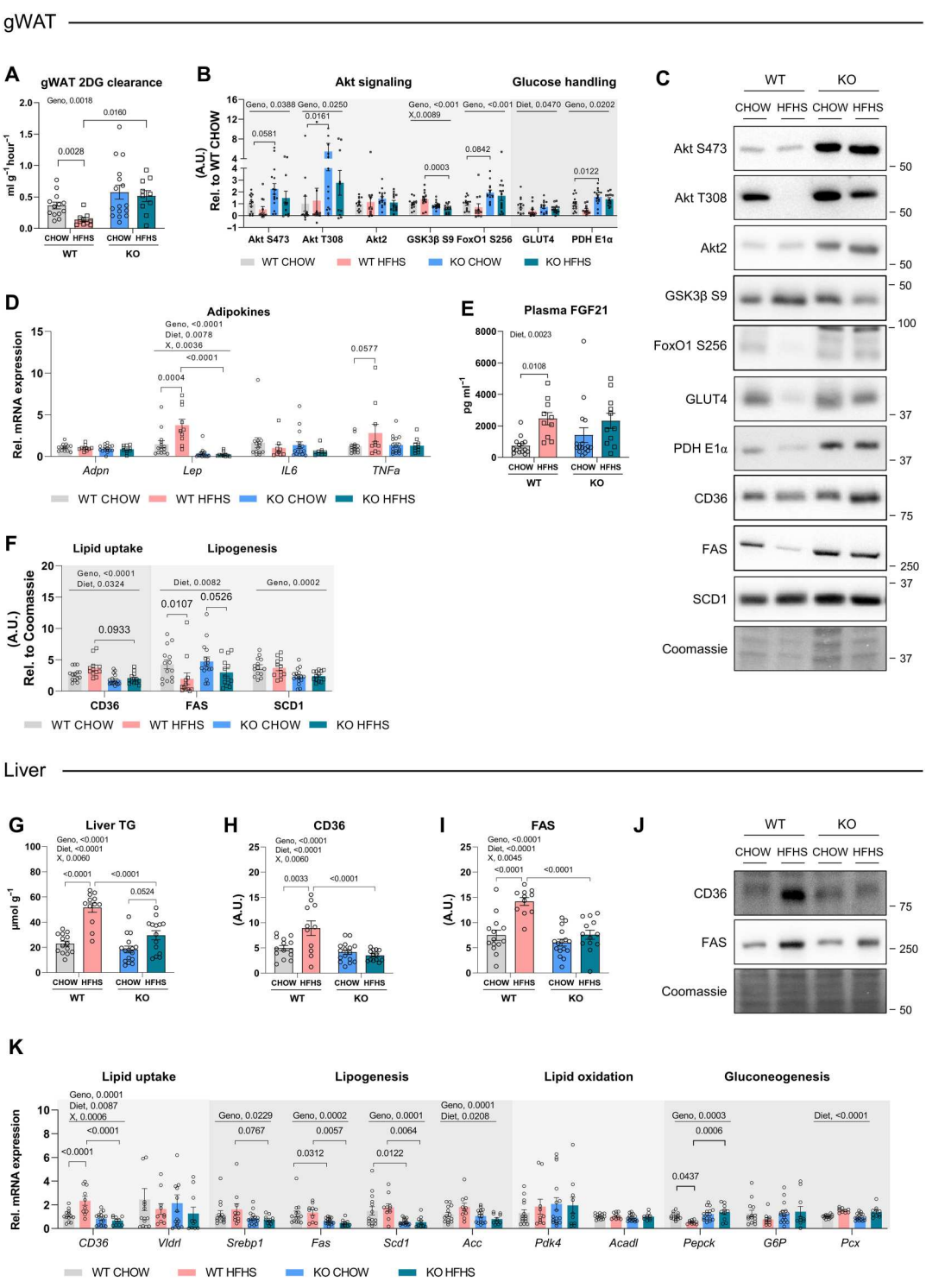

Fig. 5. TNIK deficiency elevates insulin-stimulated glucose uptake in WAT via enhanced insulin signaling and prevents diet-induced hepatic steatosis. The effect of *Tnik* knockout (KO) and chow or high-fat high-sucrose (HFHS) diet on insulin-stimulated (**A**) 2DG clearance in gWAT; (**B**) content of proteins involved in Akt signaling (Akt S473, Akt T308, Akt2, FoxO1 S256, and GSK3β S9) and glucose handling (GLUT4 and PDH E1α); (**C**) representative blots; (**D**) mRNA levels of gWAT adipokines [adiponectin (*adpn*) and leptin (*Lep*)] and inflammatory cytokines (*IL6* and *TNFa*); (**E**) plasma FGF-21 concentration; (**F**) content of proteins representative of gWAT lipid uptake (CD36) and lipogenesis (FAS and SCD1); (**G**) liver TG levels; (**H**) liver CD36 protein content; (**I**) liver FAS protein content; (**J**) representative blots; and (**K**) mRNA levels representative of liver lipid uptake (*CD36* and *Vldr*), lipogenesis (*Srebp1*, *Fas*, *Scd1*, and *Acc*), lipid oxidation (*Pdk4* and *Acadl*), and gluconeogenesis (*Pepck*, *G6P*, and *Pcx*). Data are shown as means + SEM, including individual values where applicable. Statistical significances were calculated using two-way ANOVA in conjunction with Šídák's multiple comparisons test (A, B, D, E, G, H, I, and K) or Tukey's multiple comparisons test (F). Data are shown as means + SEM, including individual values where applicable.

GSK3β at S9 was, however, reduced in *Tnik* KO gWAT (Fig. 5, B and C). Similar to skeletal muscle, total GLUT4 content was not changed in *Tnik* KO gWAT, but PDH E1α was up-regulated (Fig. 5, B and C).

The WAT is one of the largest endocrine organs in the body owing to its ability to release bioactive molecules known as adipokines to evoke a systemic response to energetic status, feeding behaviors, and inflammation (*25*, *26*). We found lower gWAT *leptin* and tumor necrosis factor–α (*TNFa*) mRNA expression in *Tnik* KO mice, particularly on HFHS, likely due to the lower fat mass (Fig. 5D). gWAT adiponectin mRNA levels were similar between groups (Fig. 5D). The plasma levels of the metabokine fibroblast growth factor 21 (FGF-21), known to regulate BW through enhanced insulin sensitivity and energy expenditure (*27*–*30*), were not changed between WT and *Tnik* KO mice (Fig. 5E). These results indicate that TNIK depletion potentially reduces the release of the proinflammatory cytokines leptin and *TNFa* derived from obese adipose tissue.

It is well established that obesity and metabolic dysregulation can result from an imbalance between fat uptake, synthesis, and catabolism in WAT (*31*). Thus, we determined the expression of genes encoding for key regulators of lipid uptake and lipogenesis. The content of proteins regulating lipid uptake (CD36) and lipogenesis (SCD1, but not FAS) were significantly down-regulated in *Tnik* KO mice (Fig. 5F). These findings suggest that TNIK depletion affects lipid metabolism through down-regulation of lipid uptake and potentially lipogenic programs in gWAT, which is in line with the reduced fat mass in *Tnik* KO mice.

Loss of TNIK prevents hepatic steatosis in response to HFHS diet

Obesity leads to lipid accumulation in numerous nonadipose tissues, including the liver, which further contributes to peripheral insulin resistance (*32*). Thus, we investigated the effects of global TNIK depletion on diet-induced hepatic triglyceride (TG) accumulation.

In WT mice, HFHS diet led to a 2.2-fold increase in liver TG. *Tnik* KO mice were highly protected from liver TG accumulation on HFHS diet (Fig. 5G). This was accompanied by decreased protein and/or mRNA levels of CD36, FAS, *Srebp1*, and *Scd1* (Fig. 5, H to K), while the expression of lipogenesis (*Acc*) and lipid oxidation genes (*Pdk4* and *Acadl*) were reduced or unchanged in *Tnik* KO mice (Fig. 5K). Thus, the protection from hepatic steatosis by TNIK depletion could be mechanistically conferred, at least in part, through reduced lipid uptake and particularly lipogenesis. We also observed that cytosolic *Pepck* was elevated in liver of the *Tnik* KO mice (Fig. 5K), indicative of elevated capacity for gluconeogenesis. These results show that loss of TNIK modulates hepatic gluconeogenic and lipogenic programs that could confer the hepatoprotective effects against HFHS diet.

TNIK variants correlate with obesity- and T2D-related traits

Our intriguing data from two animal models prompted us to test whether the results could provide translational value for human patients with obesity and T2D. For that, we used the T2D Knowledge Portal (T2DKP; https://t2d.hugeamp.org) database, containing 292 datasets and 326 traits, to explore GWAS datasets for the association of TNIK with T2D and related traits. As shown in Fig. 6A, strong significant associations ($P < 0.001$) between variants of TNIK with random and fasting glucose, HbA1c, body mass index, T2D, and TGs have been detected.

We also conducted a human case-control study within the UK Biobank, containing genetic and phenotypic data of >500,000 individuals aged 40 to 69 years, to assess the effects of predicted loss of function (pLOF) in TNIK. As shown in Fig 6B, we found significant associations between pLOF carrier status and recent poor appetite or overeating (pLOF: $P = 3.47 \times 10^{-5}$, $\beta = 2.36 \times 10^{-2}$), body fat percentage (pLOF: $P = 1.72 \times 10^{-4}$, $\beta = 1.67 \times 10^{-2}$), and blood glucose (pLOF: $P = 0.000331$, $\beta = 0.899428$). In conclusion, our human case-control study together with the larger GWAS data points towards a hitherto unrecognized role for TNIK in T2D and obesity.

DISCUSSION

Across flies, mice, and humans, we identify TNIK as a crucial regulator of glucose and lipid metabolism, inferred via four major findings. First, genetic ablation of *Tnik*/*msn* in mice/flies rewired cellular metabolism and led to down-regulation of HFHS/HSD-induced lipogenic programs. Second, *Tnik* KO mice showed increase in ambulant activity and remarkable protection against diet-induced obesity, peripheral insulin resistance, and hepatic lipid accumulation. Third, mechanistic insights revealed enhanced insulin signaling and elevated capacity for glucose and lipid handling in several tissues, including skeletal muscle, WAT, and the liver. Notably, these effects were not cell autonomous in skeletal muscle. Last, human variants and loss of function variants of TNIK strongly associated with body mass index, fasting glucose, T2D, body fat, and feeding behavior, providing translational value of the diet-induced fly and mouse models of TNIK deficiency.

The major role for TNIK in metabolic control was evident as *Drosophila* lacking *TNIK*/*msn* were intolerant to dietary sugars and exhibited wide-spread changes in sugar-induced metabolism revealed by whole-body metabolomics of HSD-fed larvae. Notably, fatty acid levels, as well as the lipogenic genes, *Fas* and *Acc*, were markedly down-regulated during sugar feeding in *msn* RNAi animals, suggesting that TNIK controls the metabolic flux of dietary sugars into lipids. That was corroborated by the observation that the metabolite DHAP, situated at the metabolic junction between glycolysis and lipid synthesis (*16*), was one of the top metabolites decreased by sugar in an *msn*-dependent manner. DHAP also activates the nutrient and energy sensor mTORC1 (*16*, *33*). Thus, TNIK could, via DHAP, be implicated in the ability of mTORC1 to sense glucose availability and to further play a critical role in postprandial de novo lipogenesis (*16*). The protein sensor and regulator of DHAP have been hitherto unknown, but our data suggest that it might be TNIK/msn, which is an enticing question to be tackled in future studies.

Flies lacking *msn* showed almost complete lethality regardless of the diet. This contrasted with the phenotype of *Tnik* KO mice that showed a metabolically healthy phenotype. A likely explanation is that *msn* is the only ortholog for the germinal center kinase IV subfamily of Ste20 kinases in flies, whereas mice and humans express three: *TNIK*, misshapen-like kinase 1 (*MINK1*), and *MAP4K4*. Further studies on mammalian *MINK1* and *MAP4K4* are required to unravel their role and possible redundancy in TNIK-regulated metabolic processes.

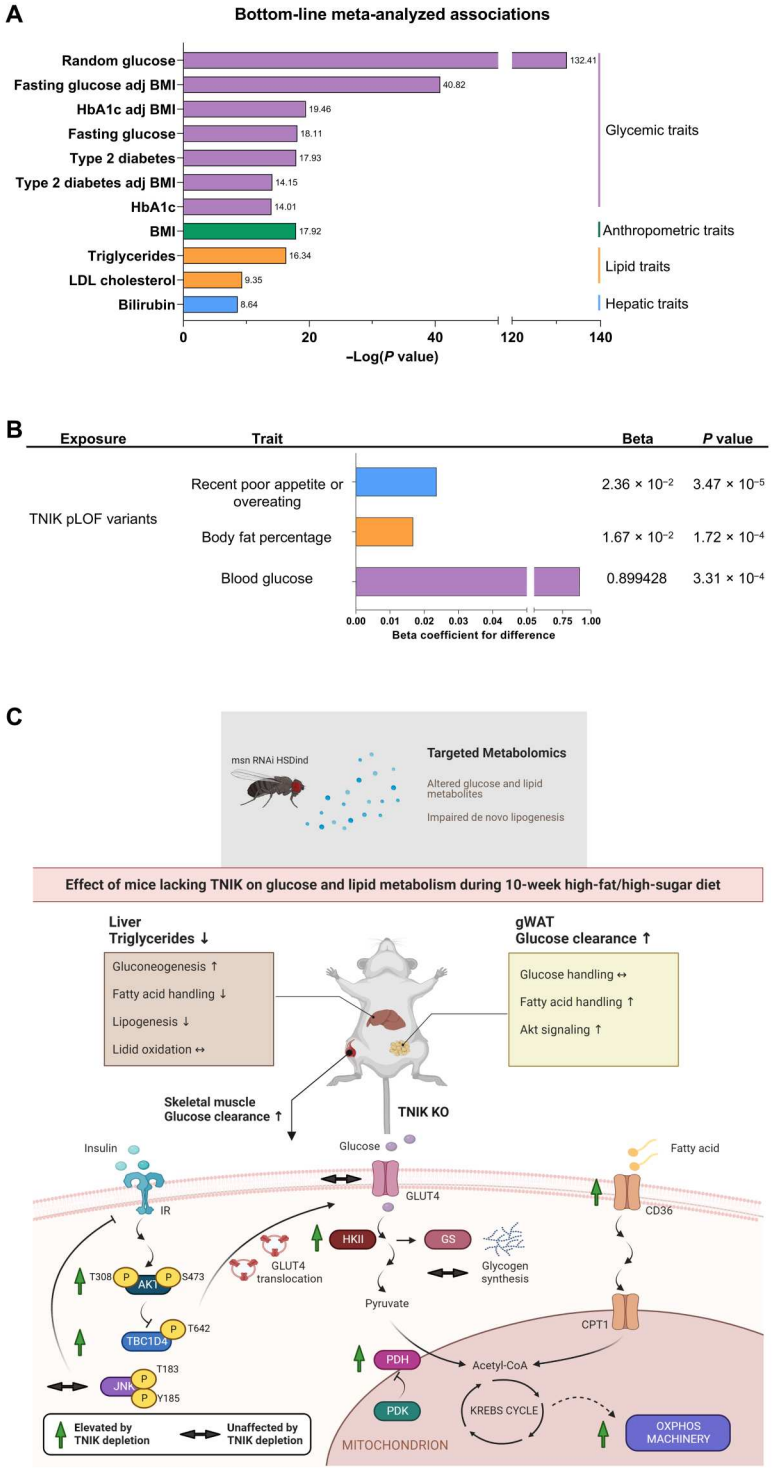

Fig. 6. TNIK variants correlate with T2D-related traits. (**A**) Bottom-line meta-analyzed association between variants of TNIK and metabolic traits extracted from T2DKP (https://t2d.hugeamp.org). (**B**) Association between TNIK pLOF carrier status and poor appetite and overeating, body fat percentage, and blood glucose in UK Biobank participants calculated from linear regression models of association. Point estimates are shown as bars. (**C**) Illustration of findings obtained in the current study. The illustration was created using BioRender.

Untargeted plasma metabolomics revealed an increase in specific plasma fatty acids, including myristic acid (a saturated fatty acid), oleate (a monounsaturated fatty acid), and gamma-linolenic acid and docosahexaenoic acid (both polyunsaturated fatty acids) in *Tnik* KO mice, indicative of increased lipolysis or diminished lipid uptake into adipose tissue. These observations suggest that TNIK is a conserved key regulator of lipid homeostasis by inhibiting lipid uptake and de novo lipogenesis, altogether preventing the storage of lipids as fat.

A second major discovery was that *Tnik* KO mice showed remarkable protection against diet-induced obesity, peripheral insulin resistance, and hepatic TG accumulation. The obesity-resistant phenotype was evident in both female and male mice. Sexual dimorphism in response to metabolic challenges has been frequently reported in mouse models with diet-induced obesity (*34*–*36*). Our findings underscore that TNIK′s effects on body weight and composition, glucose homeostasis, and insulin responsiveness occur independently of sex. A desirable goal of obesity treatment is enhancing insulin sensitivity, as insulin resistance is the first defect detectable in individuals at high risk for T2D (*37*). Because increased physical activity or exercise training of mice partially protects against fat accumulation and improves insulin sensitivity (*20*), the increase in energy expenditure of the *Tnik* KO mice largely contributes to the obesity-resistant phenotype. However, the phenotype of the *Tnik* KO mice can be dissociated from an exercise training phenotype that is usually accompanied by increased exercise capacity (*19*), grip strength (*38*), and bone volume fraction (*21*), which was similar to WT mice. A potential role for TNIK in incentive motivation is an interesting avenue to explore further, given that sedentary behavior contributes to the development of obesity and T2D.

Notably, the *Tnik* KO mice exhibited an exceptionally efficient glucose metabolism that facilitated the rapid clearance of glucose from circulation, evident during the insulin and pyruvate tolerance test. In addition, the potential inhibition of hormonal counterregulation in response to an insulin challenge was an unexpected observation yet raised a potential role for TNIK in not only modulating insulin but also hormonal counterregulation.

Weight loss is one of the strongest predictors of improved insulin sensitivity, which is corroborated by our mechanistic insights into the obesity-resistant and insulin-sensitive phenotype of *Tnik* KO mice. The mechanisms that could account for the obesity-resistant and insulin-sensitive phenotype of *Tnik* KO mice were associated with substantial alterations in insulin signaling, glucose, and lipid metabolism in the gWAT, liver, and skeletal muscle. Chow-fed *Tnik* KO mice had increased glucose and lipid oxidation rates, suggesting that diet-derived fat was preferentially oxidized to support their increased energy expenditure. While we did not measure tissue fatty acid uptake directly, the expression of the lipid transporter CD36 was up-regulated in skeletal muscle. This may point towards an increased lipid uptake and utilization in muscle to provide substrates for the increased ambulant activity in *Tnik* KO mice. In parallel, genes implicated in lipid uptake and, potentially, de novo lipogenesis in *Tnik* KO gWAT were decreased, consistent with a switch towards fat utilization versus storage in *Tnik* KO mice.

The lack of weight gain in *Tnik* KO mice, despite an observed positive energy balance, was an unexpected finding. This phenomenon could potentially be attributed to various factors, such as nutrient absorption capacities, potential methodological inaccuracies, or stress induced by housing mice in metabolic chambers.

Moreover, TNIK deficiency resulted in a protection against HFHS-induced hepatic steatosis and inflammation, as evidenced by marked reduction of lipid accumulation concomitant with reduced lipid uptake via CD36, and lipogenesis via FAS, SREBP1, and SCD1 in HFHS *Tnik* KO mice. Although the phenotype of the *Tnik* KO mice could be dissociated from an exercise-trained phenotype, many of the molecular adaptations are concordant with exercise-trained human skeletal muscle, including elevated protein content of insulin signaling and glucose-handling proteins Akt2, TBC1D4, HKII, and GS (*39*). *Tnik* KO mice also likely have an intrinsically high oxidative capacity. This was indicated by the increased energy expenditure and ambulant activity during the dark period accompanied by elevated muscle OXPHOS protein abundance. The reduced fat deposition combined with the higher oxidative capacity in TNIK-deficient skeletal muscle may account for the obesity-resistant phenotype and elevated insulin sensitivity and glucose clearance.

However, our findings in siRNA TNIK KD C2C12 myotubes suggest that the systemic effects observed with *Tnik* KO are unlikely to be driven by direct effects of skeletal muscle TNIK. Thus, the effects of TNIK on insulin sensitivity are due to low adiposity and/or other systemic effects of *Tnik* KO in nonmuscle tissue. Because of TNIK′s prominent expression in the brain, it is plausible that TNIK exerts its primary effects on brain function, followed by secondary effects in the peripheral tissues. The direct effect of TNIK in the brain on food intake regulation, energy expenditure, and body weight are unknown, yet our findings suggest that function of TNIK could play a critical role in the regulation of whole-body energy homeostasis. Our findings open exciting avenues for future research to improve our understanding of the molecular mechanisms underlying the regulation of energy homeostasis.

Our final finding was that human variants of *TNIK* are strongly associated with body mass index, fasting glucose, and T2D, while pLOF variants of *TNIK* are strongly linked to feeding behavior, body fat percentage, and blood glucose. Collectively, these findings establish a strong translational ground for TNIK as a conserved regulator of glucose and lipid metabolism in obesity, also in humans.

Our study has limitations that should be acknowledged when interpreting the results. First, once the metabolic tests commenced, the mice did not gain any more weight, and there were differences between fasting glucose and insulin-stimulated glucose excursion curves, which may have been due to frequency of experiments, related stress, and the use of anesthesia (pentobarbital) and analgesics (lidocaine) during the terminal experiment. Pentobarbital and lidocaine have been shown to increase insulin secretion and impair glucose tolerance (*40*) and may have contributed to the discrepancies in blood glucose in awake and anesthetized mice. Although in accordance with our animal license, these limitations highlight the need for further research to fully understand the impact of experimental conditions on the results.

Another limitation of our study is that we did not measure TNIK activity. In the literature, a few TNIK downstream targets have been suggested, including JNK T183/Y185 (*6*), which we did not find to be regulated in TNIK-deficient skeletal muscle. That discrepancy could be explained by possible redundant actions of mitogen-activated protein kinase kinase 4 (MKK4) and MKK7 that have also been shown to catalyze the phosphorylation of JNK at T183/Y185 (*30*, *31*). Another limitation is that our study identifies TNIK within the context of obesity and prediabetes and not T2D directly. While

the GWAS point towards it, mechanistic studies must include diabetic animal models to conclude that TNIK could be a crucial player in both obesity and T2D.

The advent of human GWAS studies has led to the identification of thousands of loci contributing to metabolic diseases such as obesity and T2D. However, many variants identified have shown to either not be the causal variant or only modestly affecting disease phenotype (*4*). Here, we build upon a GWAS-derived gene discovery (*7*) and combine it with a post-GWAS systematic investigation of TNIK′s mechanistic role in obesity and diet-induced metabolic dysregulation.

Together, our study identifies TNIK as a conserved and hitherto unrecognized critical player in glucose and lipid metabolism (Fig. 6C). The concept that TNIK/msn is sensitive to glucose, and likely at the junction of lipid metabolism, opens perspectives for investigations on metabolic regulation of TNIK in obesity and T2D and eventually therapeutic targeting of TNIK signaling.

MATERIALS AND METHODS

Drosophila studies

Fly food, stocks, and husbandry

RNAi lines (60,100 kk control and 101,517 kk msn) were obtained from the Vienna *Drosophila* Resource Center. All stocks were maintained at +25°C on medium containing 1% (w/v) agar, 1.3% (w/v) dry baker′s yeast, 8% (w/v) molasses, 4% (w/v) corn flour, 0.6% (v/v) propionic acid, and 1.2% (v/v) Nipagin. The experiments took place at +25°C, 65% humidity under a 12-hour light/12-hour dark cycle. For defined nutrient studies, larvae were grown on defined food containing 0.5% (w/v) agar, 2.4% (v/v) Nipagin, 0.7% (v/v) propionic acid, and 10% (w/v) dry baker′s yeast (HPD). For HSD, 20% (w/v) sucrose was added. First-instar larvae were collected from apple juice plates [33.33% (v/v) apple juice, 1.75% (w/v) agar, 2.5% (w/v) sucrose, and 2% (v/v) Nipagin]. Larvae were grown on defined diets at controlled density (30 larvae per vial).

Metabolic assays

Hemolymph glucose was measured from third-instar prewandering larvae using a GAGO-20 kit (Sigma-Aldrich) as described previously (*41*).

RNA extraction and quantitative polymerase chain reaction

Five second-instar larvae per sample were homogenized and RNA was extracted using a NucleoSpin RNA kit (Macherey-Nagel) according to the manufacturer′s protocol. Reverse transcription was performed with an equal amount of RNA (RevertAid H Minus First Strand cDNA Synthesis Kit, Thermo Scientific). Quantitative reverse transcription polymerase chain reaction (qRT-PCR) experiment was conducted using Maxima SYBR Green qPCR Master Mix (2×) (Fermentas) in the LightCycler 480 Real-Time PCR System (Roche) in three technical replicates. The primers used for qPCR are listed in table S1.

Mouse studies

Animals

Homozygous *Tnik* KO mice were generated as previously described (*17*) and backcrossed to C57BL/6 background in our own animal facilities. B6 JM8.N3 ES cells (*42*) were transfected with the targeting construct PRPGS00070_B_G02 (source: Knockout Mouse Project). Transgenic mice were crossed to FLP-deleter mice and subsequently to CRE-deleter mice to generate *Tnik* KO mice by deleting exon 6. All mice were maintained under a 12-hour light/12-hour dark photocycle at 22° ± 2°C with nesting material. The female mice were group-housed. Male mice were single-housed to reduce aggression and potential further injuries when they were fighting despite our awareness of the potential for depressive behavior induced by single housing.

Until approximately 20 weeks of age, mice received a rodent chow diet (Altromin no. 1324, Chr. Pedersen, Denmark) and water ad libitum. For dietary interventions, 13- to 15-week-old littermate mice were randomized into test groups and given ad libitum access to either a rodent chow diet (Altromin no. 1324, Chr. Pedersen, Denmark) and water or an HFHS diet [45% kcal from fat, 35% kcal from carbohydrates, and 20% kcal from protein (Research Diets, no. D12451)] and 10% sucrose water for 10 weeks. Body weights were measured at weeks 2, 4, 8, 9, and 10 of the diet intervention study. All experiments were performed using animals at 14 to 30 weeks of age (schematically illustrated in Fig. 2B).

Food and sucrose water consumption

Except for the male mice that were single-housed because of fighting, individual records of feeding were not possible because of animal welfare concerns. Instead, food (and sucrose water consumption, when applicable) was estimated by measuring the total amount consumed by each group of mice, separated by genotype, and dividing it by the number of mice within the group. It was assumed that food intake was evenly distributed among mice.

Genotyping

Mouse genotyping was performed as previously described (*43*) using qPCR on DNA from ear punches with the following primers: WT, 5′-CCA TTA ACT CTC TCG CCT CTT CAT TCC-3′ and 5′-AAT CAC TTT GTG CTG GTG CAG GT-3′ and KO, 5′-CGC CGT ATA GCA TAC ATT ATA CGA AGT T-3′ and 5′-CAT CAT GTC AGC AGT GAT ACA AAC CA-3′.

Body composition

Total fat and lean body mass were measured at indicated time points (Fig. 2B) by nuclear magnetic resonance using an EchoMRI (USA).

Indirect calorimetry

After a 3-day acclimation period in metabolic cages, male mice underwent indirect calorimetry to measure their oxygen consumption (VO_2) and CO_2 production (VCO_2). In addition, their ambulant activity (number of beam breaks) and chow food intake were recorded for 3 days using a CaloSys apparatus (TSE Systems, Bad Homburg, Germany). Energy expenditure was estimated by multiplying oxygen consumption with O_2 (20 kJ/liter). Energy balance was determined by subtracting the energy expenditure from the energy intake. Fatty acid oxidation rates were calculated as $VO_2 \times 19$ kJ/liter $O_2 \times \{[1 - (VCO_2/VO_2)]/0.3\}$ and carbohydrate oxidation rates a $VO_2 \times 21$ kJ/liter $O_2 \times \{[(VCO_2/VO_2) - 0.7]/0.3\}$. Relative fatty acid oxidation rates in percent of total oxidation were calculated as $[1 - (VCO_2/VO_2)]/0.3 \times 100$ and relative carbohydrate oxidation rates in percent of total oxidation as $[(VCO_2/VO_2) - 0.7]/0.3 \times 100$.

Exercise capacity tests

Tnik KO and WT mice were acclimatized to the treadmill on three consecutive days at a speed of 0.16 m/s and incline of 10° for 5 min the first day and 10 min the following days. On the experimental day, the mice started running at 0.16 m/s for 5 min at an incline of 10° followed by a gradual increase in speed every minute with 0.02 m/s until exhaustion. The test was stopped when the mouse

has reached its maximal running capacity by failing to keep up with the treadmill despite motivational efforts by the researcher.

Forelimb/hindlimb grip strength test

To determine forelimb/hindlimb (four paws) grip strength measurements, mice grasped the bar mounted on the force gauge. The system is either horizontally or vertically oriented. The mouse's tail is slowly pulled back (horizontally oriented force gauge) or down (vertically oriented force gauge). Tension is recorded by the gauge at the time the mouse releases its forepaws from the bar. Three consecutive measurements are performed interspersed by 1 min resting intervals.

Micro–computed tomographic scanning

Mice were euthanized at 31 to 35 weeks of age, and tibia were collected, fixed in 10% formalin solution for 48 hours at 4°C, followed by storage in phosphate-buffered saline at 4°C until analysis. A high-resolution micro–computed tomographic (μCT) system (vivaCT 40, SCANCO Medical, Bruttisellen, Switzerland) was used to scan the proximal tibia of mice, resulting in a three-dimensional (3D) reconstruction of cubic voxel sizes of 10.5 μm by 10.5 μm by 10.5 μm. For each 3D image, a dataset consists of 150 μCT slide images, and 70 (700 μm) slide images were used for analysis of the trabecular tissue to determine bone volume fraction defined as BV/TV.

Metabolic tests

We subjected a subset of mice to several metabolic tests to assess pyruvate, glucose, or insulin tolerance, which commenced at 7, 8, and 9 weeks of the diet intervention study, respectively. For pyruvate and glucose tolerance tests, mice were fasted for 5 hours, and for insulin tolerance tests, mice were fasted for 3 hours from 7:00 a.m. Blood was drawn from the tail during the experiment. Resting blood samples were taken 30 min before the intraperitoneal injection of sodium pyruvate (P2256, Sigma-Aldrich, St. Louis, MO, USA) or *d*-mono-glucose (2 g kg^{-1} BW) or insulin 0.3 IU kg^{-1} BW (Actrapid, Novo Nordisk, Bagsværd, Denmark). Tail blood glucose concentrations were measured with a glucometer (Bayer Contour, Bayer, Münchenbuchsee, Switzerland) at 0, 20, 40, 60, and 90 min for the glucose and insulin tolerance test and additionally at 120 and 180 min for the pyruvate tolerance test.

Notably, the insulin tolerance test had to be stopped before the 60-min time point for two chow-fed and two HFHS-fed *Tnik* KO mice and before the 90-min time point for an additional four chow-fed and three HFHS-fed *Tnik* KO mice because of hypoglycemia (blood glucose, <1.7 mM). Thus, blood glucose was not measured for these mice at all the time points. During the pyruvate tolerance test, the test had to be stopped after the 90-min time point and the 120-min time point for one HFHS-fed *Tnik* KO mouse each because of hypoglycemia.

To measure glucose-stimulated plasma insulin concentration at time points 0 and 20 min, tail vein blood samples were collected in a capillary tube (50 μl), centrifuged at 14,200*g* for 5 min at 4°C, and plasma was collected and stored at −80°C. Insulin concentration was determined in duplicate using the Mouse Ultrasensitive Insulin ELISA Kit (#80-INSTRU-E10, ALPCO Diagnostics) to the manufacturer's instructions.

For the metabolic tests, pooled glycemic excursions for both sexes are shown in Fig. 3 to better detect genotype-specific differences. Sex-specific glycemic excursion curves and related measures are shown in fig. S4. The iAUC or incremental area over the curve from the basal blood glucose concentration was determined using the trapezoid rule.

Insulin-stimulated 2DG uptake

The protocol for measuring insulin-stimulated 2DG uptake has also been described in detail elsewhere (*44*). The mice were fasted for 3 hours before being anesthetized for 15 min with 1:10 lidocaine:pentobarbital (6 mg of pentobarbital sodium 100 g^{-1} BW) by intraperitoneal injection. Insulin-stimulated 2DG uptake into peripheral tissues was measured by retro-orbital injection of 2DG (PerkinElmer) diluted in saline, containing 2DG (66.7 μCi/ml, 6 μl g^{-1} BW) and insulin at a concentration of 0.3 U/kg BW (Actrapid, Novo Nordisk, Bagsværd, Denmark). The blood glucose concentration was measured via the tail vein at 0, 3, 6, 9, and 12 min (Bayer Contour, Bayer, Münchenbuchsee, Switzerland). At 12 min, the mice were euthanized via cervical dislocation, and the tissues were excised, weighed (skeletal muscle and gWAT), and snap-frozen in liquid nitrogen. The samples were stored at −80°C for further processing/analyses. Plasma was collected via punctuation of the heart, where blood was drawn, centrifuged, and stored at −80°C. A single determination of insulin concentration was conducted using the Ultra-Sensitive Mouse Insulin ELISA Kit (#80-INSTRU-E10, ALPCO Diagnostics) in accordance with the manufacturer's instructions. Plasma FGF-21 concentrations were measured using the Mouse/Rat FGF-21 Quantikine ELISA Kit (R&D Systems) according to the manufacturer's instructions.

Tissue-specific 2DG–6-phosphate accumulation was measured as described previously (*45*, *46*). To determine 2DG clearance from the plasma into the skeletal muscles (gastrocnemius, TA, and soleus) or gWAT, tissue-specific 2DG–6-P was divided by the AUC of the plasma-specific 2DG activity at 0 and 12 min. To estimate tissue-specific glucose uptake (glucose uptake index), clearance was multiplied by the average blood glucose levels at 0, 3, 6, 9, and 12 min. Tissue-specific 2DG clearance was related to the weight of the analyzed tissue and time.

Cell culture maintenance

The C2C12 WT cell line was cultured in Dulbecco's modified Eagle's medium (DMEM) supplemented with 10% fetal bovine serum and 1% antibiotic-antimycotic solution. The cells were maintained at 37°C in a humidified incubator with 5% CO_2.

siRNA-mediated transfection

For seeding and siRNA-mediated transfection, C2C12 WT cells were seeded at a density of 20,000 cells per well in a 12-well plate in the evening. In the following morning, siRNA transfection was performed using either Control siRNA-A (siScr; 70 nM; sc-37007, Santa Cruz Biotechnology) or TNIK siRNA (siTNIK; 70 nM; sc-154540, Santa Cruz Biotechnology) using jetPRIME siRNA transfection reagent. The transfection was repeated 48 hours later. Once the cells reached 90 to 100% confluence, the medium was replaced with differentiation medium containing DMEM supplemented with 2% horse serum and 1% antibiotic-antimycotic solution. The differentiation medium was replaced every 2 days, and the cells were maintained in the differentiation medium for a total of 7 days.

Insulin-stimulated intracellular signaling in C2C12 myotubes

On day 7 of differentiation, the cells were starved for 3 hours using serum-free DMEM supplemented with 1% antibiotic-antimycotic solution, followed by 100 nM insulin stimulation for 15 min. The cells were then harvested and lysed in ice-cold homogenization buffer [10% glycerol, 1% NP-40, 20 mM sodium pyrophosphate,

150 mM NaCl, 50 mM Hepes (pH 7.5), 20 mM β-glycerophosphate, 10 mM NaF, 2 mM phenylmethylsulfonyl fluoride, 1 mM EDTA (pH 8.0), 1 mM EGTA (pH 8.0), 2 mM Na_3VO_4, leupeptin (10 μg ml^{-1}), aprotinin (10 μg ml^{-1}), and 3 mM benzamidine]. The lysates were centrifuged at 9000*g* for 10 min at 4°C, and the supernatants were collected for further analysis. Four independent experiments were conducted.

Quantitative reverse transcription polymerase chain reaction

RNA was extracted from mouse liver using the phenol chloroform method. Briefly, tissues were homogenized using TissueLyser (QIAGEN) in 1 ml of TRIzol (Sigma-Aldrich). Chloroform was added. The samples were mixed and centrifuged, and the aqueous phase was transferred to a fresh tube. RNA was precipitated at −20C for 20 min after the addition of isopropanol and 15 μg of glycogen (AM9510, Life Technologies) per 1 ml of TRIzol initially used. The samples were then centrifuged to pellet the RNA. The pellet was washed with ethanol two times to avoid salt and phenol contamination. The RNA was lastly resuspended in nuclease-free water. For gWAT, RNA was extracted using phenol-chloroform followed by column-based RNA purification method (RNeasy Midi kit, QIAGEN). Briefly, the aqueous phase obtained after chloroform addition was mixed with 1:1 70% ethanol and loaded on silica-membrane columns. The extraction was then done following the manufacturer′s instructions. RNA concentration and purity were assessed by absorbance at 260 and 280 nm using NanoDrop One (Thermo Fisher Scientific, Waltham, MA). RNA (500 ng) was reverse-transcribed to cDNA using the High-Capacity cDNA RT Kit (Thermo Fisher Scientific). Briefly, a mix of random primers, deoxynucleotide triphosphate, RT buffer, and MultiScribe Reverse Transcriptase enzyme was added to the RNA samples. Reverse transcription was performed for 10 min at 25°C and then 120 min at 37°C to allow cDNA polymerization. Then, samples were heated for 5 min at 85°C to stop the reaction. Gene expression was determined by real-time qPCR using a LightCycler 480 (Roche) and Precision Plus qPCR Master Mix (Primer Design Ltd). Results were then analyzed using the $\Delta\Delta C_t$ method using an average of at least two housekeeping genes as control. The primers used for qPCR are listed in table S1.

Muscle glycogen measurement

Muscle glycogen content was measured as glycosyl units after acid hydrolysis, and muscle glycogen was determined from neutralized perchloric acid extracts and measured spectrophotometrically at 340 nm (Hitachi 912 Automatic Analyzer, Böhringer, Germany) (*47*).

Liver TG accretion

Liver TG content was measured in 15 to 20 mg of tissue as described (*48*). Liver tissue was homogenized in ice-cold extraction buffer (0.15 M natriumacetate in 25% Triton X-100) for 1 min, heated at 97°C for 3 min, and then centrifuged at 9000*g* for 10 min. Supernatants were collected, and TG content was photometrically measured using the Pentra C400 analyzer (Horiba, Japan).

Lysate preparation and immunoblotting

Skeletal muscle, adipose tissue, and liver samples were pulverized in liquid nitrogen and homogenized for 1 min at 30 Hz using a TissueLyser II bead mill (QIAGEN, USA) in ice-cold homogenization buffer [10% glycerol, 1% NP-40, 20 mM sodium pyrophosphate, 150 mM NaCl, 50 mM Hepes (pH 7.5), 20 mM β-glycerophosphate, 10 mM NaF, 2 mM phenylmethylsulfonyl fluoride, 1 mM EDTA (pH 8.0), 1 mM EGTA (pH 8.0), 2 mM Na_3VO_4, leupeptin (10 μg ml^{-1}), aprotinin (10 μg ml^{-1}), and 3 mM benzamidine]. Following end-over-end rotation for 30 min at 4°C, the samples were centrifuged at 14,200*g* for 20 min at 4°C. The supernatants (lysate) were collected afterward. The centrifugation was repeated twice for adipose tissue samples. All samples were stored at −80°C.

Lysate protein concentration was determined colorimetrically using the bicinchoninic acid method and bovine serum albumin (BSA) as a protein standard (Pierce BCA Protein Assay Kit, Thermo Fisher Scientific, Rockford, IL, USA). Total protein and protein phosphorylation were determined by standard immunoblotting techniques loading equal amounts of protein solubilized in sample buffer [340 mM tris (pH 6.8), 225 mM dithiothreitol, 11% (w/v) SDS, 20% (v/v) glycerol, and 0.05% (w/v) bromophenol blue]. Polyvinylidene difluoride membranes (Immobilon Transfer Membrane, Merck KGaA, Darmstadt, Germany) were blocked in 2% milk or 3% BSA diluted in tris-buffered saline–Tween 20 (blocking buffer) for 15 min at room temperature. Membranes were incubated with primary antibodies in blocking buffer, presented in table S2, overnight at 4°C, followed by incubation with horseradish peroxidase–conjugated secondary antibody diluted in blocking buffer for 60 min at room temperature. The specificity of the anti-TNIK antibody was tested in WT and KO skeletal muscle, gWAT, and liver (fig. S5, J and L).

Bands were visualized using the Bio-Rad ChemiDoc MP Imaging System and enhanced chemiluminescence (ECL+, Amersham Biosciences). Coomassie Brilliant Blue staining was used as a control to assess total protein loading and transfer efficiency (*49*) by quantifying the whole lane, and for each sample set, a representative membrane from the immunoblotting is shown. Coomassie Brilliant Blue staining was used for normalization only in gWAT samples. The same Coomassie Brilliant Blue staining is presented for proteins analyzed when derived from the same sample set. Band densitometry was carried out using ImageLab (version 4.0). For each set of samples, a standard curve was loaded to ensure quantification within the linear range for each protein probed.

Metabolomics

Targeted metabolomics liquid chromatography–mass spectrometry profiling analysis

Metabolites were extracted from 10× third-instar *Drosophila* larvae using 2 ml of Precellys homogenization tube (Bertin Technologies) with 2.8-mm ceramic (zirconium oxide) beads with 400 μl of cold extraction solvent (acetonitrile:methanol:M, 40:40:20). Subsequently, samples were homogenized using tissue homogenizer (Bertin Technologies) for three cycles (30 s at 5500 rpm with 60-s pause at 4°C) followed by centrifugation at 14,000 rpm at 4°C for 5 min. For mouse plasma, metabolites were extracted from 15 μl of serum with 400 μl of cold extraction solvent and directly taken into centrifugation at 14,000 rpm at 4°C for 5 min. Supernatants were loaded into an Ostro 96-well plate (25 mg; Waters) and passed through using robotic vacuum. Filtrates were transferred into polypropylene tubes and placed into nitrogen gas evaporator to dry the solvent completely. Dried samples were suspended with 40 μl of extraction solvent and vortex for 2 min and transferred into high-performance liquid chromatography glass auto sampler vials. Two microliters of samples was injected with Thermo Vanquish UHPLC coupled with Q-Exactive Orbitrap quadrupole mass spectrometer equipped with a heated electrospray ionization (H-ESI) source probe (Thermo Fisher Scientific). A SeQuant ZIC-pHILIC

(2.1 mm × 100 mm, 5-μm particle) column (Merck) used for chromatographic separation. Gradient elution was carried out with a flow rate of 0.100 ml/min with using 20 mM ammonium hydrogen carbonate, adjusted to pH 9.4 with ammonium solution (25%) as mobile phase A and acetonitrile as mobile phase B. The gradient elution was initiated from 20% mobile phase A and 80% mobile phase B and maintained until 2 min; after that, 20% mobile phase A gradually increased up to 80% until 17 min, and then, 80% to 20% mobile phase A decreased in 17.1 min and maintained up to 24 min. The column oven and autosampler temperatures were set to 40° ± 3°C and 5° ± 3°C, respectively. Mass spectrometry equipped with an H-ESI source used polarity switching and the following setting: resolution of 35,000; spray voltages, 4250 V for positive mode and 3250 V for negative mode; sheath gas, 25 arbitrary units (A.U.); auxiliary gas, 15 A.U.; sweep gas flow, 0; capillary temperature, 275°C; and S-lens RF level, 50.0. The instrument was operated with the Xcalibur 4.1.31.9 software (Thermo Fisher Scientific). The peak integration was done with the TraceFinder 4.1 software (Thermo Fisher Scientific) for 462 metabolites. Retention times were standardized with MSMLS-1EA (Merck). The data quality was monitored throughout the run using pooled serum quality control sample interspersed throughout the run as every 10th sample. The metabolite data were checked for peak quality, relative standard deviation (%RSD), and carryover.

Metabolomics data analysis

Data (peak intensities) were analyzed in MetaboAnalyst 5.0. No samples were excluded from the data analysis. Metabolites with low response, poor chromatography (PCH), or multiple missing values were excluded from the data analysis. In MetaboAnalyst, features with >20% missing values were further removed. The remaining missing values were estimated using k-nearest neighbors (feature-wise). Interquartile range was further used for data filtering. For *Drosophila* larval data, the samples were normalized to weight, and data were log-transformed and auto-scaled. For mouse serum data, the same amount of serum (10 μl) was used for each sample, and only log transformation and auto scaling (mean-centered and divided by SD of each variable) were applied. Source data are provided as a source data file.

T2D Knowledge Portal

The T2DKP (containing 292 datasets and 326 traits) database (www.type2diabetesgenetics.org) was used to explore GWAS datasets for the association of TNIK with T2D and other glucometabolic traits.

Analysis of pLOF variants in UK Biobank

A human case-control study was conducted within the UK Biobank to assess the effects of predicted pLOF in TNIK. The UK Biobank enrolled 502,480 individuals aged 40 to 69 years. Analyses were conducted in February 2023. The UK Biobank includes genetic and clinical information, including health records, representative of the general population. All participants in the UK Biobank gave written informed consent. The study protocol and data collection have been previously described (*50*).

We examined the burden of rare pLOF variants in TNIK in whole-exome sequencing (WES) data from the UK Biobank, using Genebass. We accessed the WES dataset, of which ~450,000 participants were of European ancestry.

Detailed information on exome sequencing methodology, alignment, variant calling, and annotation in the dataset has been previously described (*51*). Quality control was conducted at a variant level on the basis of genotype read depth combined with an allele-balance filter. Additional filtering was conducted for disagreements between reported and genetically determined sex, low-sequence coverage, and high rates of heterozygosity. After quality control, ~39,500 individuals of European ancestry with exome sequence data were left for analysis.

pLOF variants were defined as variants affecting a splice site or variants resulting in a frameshift or gain of a premature stop codon. The association test was conducted using the optimal unified approach (SKAT-O), as previously described (*52*).

Associations between carrier status pLOF in TNIK and recent poor appetite or overeating, body fat percentage, and blood glucose measurements were evaluated using generalized linear models. Associations between LOF carrier status and end point were tested using logistic regression. All models were adjusted for age at enrollment, sex, assessment center, and principal components. Non-normally distributed traits were log-transformed before association. P values were corrected for multiple comparisons using a Bonferroni P value threshold of $P < 0.05/3$ ($P = 0.016$).

Ethical committee approval

All mouse experiments complied with the European Convention for the protection of vertebrate animals used for experimental and other scientific purposes (no. 123, Strasbourg, France, 1985; EU Directive 2010/63/EU for animal experiments) and were approved by the Danish Animal Experimental Inspectorate (license number: 2016-15-0201-01043).

Graphical illustrations

Graphical illustrations were created either in Adobe Illustrator or in BioRender (biorender.com), as indicated.

Statistical methods

Statistical analyses were performed using GraphPad Prism 9 (version 9.3.1). Results are presented as means ± SD or SEM, as indicated in the figure legends, with individual values shown, when feasible. Statistical tests varied according to the dataset being analyzed, and the specific tests used are indicated in the figure legends. Statistical differences were analyzed by one-way analysis of variance (ANOVA), two-way ANOVA, two-way ANOVA repeated measures (RM), or mixed effects model using diet and genotype as fixed effects. Dunnett′s multiple comparisons test, Tukey′s post hoc test, or Šídák′s multiple comparisons test was used to evaluate significant main effects of genotype, diet, or interactions in ANOVAs. P values <0.1 were considered a tendency, and P values <0.05 were considered significant.

Supplementary Materials

This PDF file includes:

Figs. S1 to S5
Tables S1 and S2
Legends for data S1 to S4

Other Supplementary Material for this manuscript includes the following:

Data S1 to S4

REFERENCES AND NOTES

1. T. Kelly, W. Yang, C. S. Chen, K. Reynolds, J. He, Global burden of obesity in 2005 and projections to 2030. *Int. J. Obes. (Lond)* **32**, 1431–1437 (2008).
2. H. Riaz, M. S. Khan, T. J. Siddiqi, M. S. Usman, N. Shah, A. Goyal, S. S. Khan, F. Mookadam, R. A. Krasuski, H. Ahmed, Association between obesity and cardiovascular outcomes: A systematic review and meta-analysis of mendelian randomization studies. *JAMA Netw. Open* **1**, e183788 (2018).
3. D. R. Leitner, G. Fruhbeck, V. Yumuk, K. Schindler, D. Micic, E. Woodward, H. Toplak, Obesity and type 2 diabetes: Two diseases with a need for combined treatment strategies—EASO can lead the way. *Obes. Facts* **10**, 483–492 (2017).
4. R. J. F. Loos, G. S. H. Yeo, The genetics of obesity: From discovery to biology. *Nat. Rev. Genet.* **23**, 120–133 (2022).
5. A. Buniello, J. A. L. MacArthur, M. Cerezo, L. W. Harris, J. Hayhurst, C. Malangone, A. McMahon, J. Morales, E. Mountjoy, E. Sollis, D. Suveges, O. Vrousgou, P. L. Whetzel, R. Amode, J. A. Guillen, H. S. Riat, S. J. Trevanion, P. Hall, H. Junkins, P. Flicek, T. Burdett, L. A. Hindorff, F. Cunningham, H. Parkinson, The NHGRI-EBI GWAS catalog of published genome-wide association studies, targeted arrays and summary statistics 2019. *Nucleic Acids Res.* **47**, D1005–D1012 (2019).
6. R. Blazev, C. S. Carl, Y. K. Ng, J. Molendijk, C. T. Voldstedlund, Y. Zhao, D. Xiao, A. J. Kueh, P. M. Miotto, V. R. Haynes, J. P. Hardee, J. D. Chung, J. W. McNamara, H. Qian, P. Gregorevic, J. S. Oakhill, M. J. Herold, T. E. Jensen, L. Lisowski, G. S. Lynch, G. T. Dodd, M. J. Watt, P. Yang, B. Kiens, E. A. Richter, B. L. Parker, Phosphoproteomics of three exercise modalities identifies canonical signaling and C18ORF25 as an AMPK substrate regulating skeletal muscle function. *Cell Metab.* **34**, 1561–1577.e9 (2022).
7. E. Havula, S. Ghazanfar, N. Lamichane, D. Francis, K. Hasygar, Y. Liu, L. A. Alton, J. Johnstone, E. J. Needham, T. Pulpitel, T. Clark, H. N. Niranjan, V. Shang, V. Tong, N. Jiwnani, G. Audia, A. N. Alves, L. Sylow, C. Mirth, G. G. Neely, J. Yang, V. Hietakangas, S. J. Simpson, A. M. Senior, Genetic variation of macronutrient tolerance in *Drosophila melanogaster*. *Nat. Commun.* **13**, 1637 (2022).
8. A. Shkoda, J. A. Town, J. Griese, M. Romio, H. Sarioglu, T. Knofel, F. Giehler, A. Kieser, The germinal center kinase TNIK is required for canonical NF-κB and JNK signaling in B-cells by the EBV oncoprotein LMP1 and the CD40 receptor. *PLOS Biol.* **10**, e1001376 (2012).
9. M. Masuda, Y. Uno, N. Ohbayashi, H. Ohata, A. Mimata, M. Kukimoto-Niino, H. Moriyama, S. Kashimoto, T. Inoue, N. Goto, K. Okamoto, M. Shirouzu, M. Sawa, T. Yamada, TNIK inhibition abrogates colorectal cancer stemness. *Nat. Commun.* **7**, 12586 (2016).
10. M. R. Banko, J. J. Allen, B. E. Schaffer, E. W. Wilker, P. Tsou, J. L. White, J. Villen, B. Wang, S. R. Kim, K. Sakamoto, S. P. Gygi, L. C. Cantley, M. B. Yaffe, K. M. Shokat, A. Brunet, Chemical genetic screen for AMPKα2 substrates uncovers a network of proteins involved in mitosis. *Mol. Cell* **44**, 878–892 (2011).
11. R. Kjobsted, J. R. Hingst, J. Fentz, M. Foretz, M. N. Sanz, C. Pehmoller, M. Shum, A. Marette, R. Mounier, J. T. Treebak, J. F. P. Wojtaszewski, B. Viollet, L. Lantier, AMPK in skeletal muscle function and metabolism. *FASEB J.* **32**, 1741–1777 (2018).
12. R. G. Baker, M. S. Hayden, S. Ghosh, NF-κB, inflammation, and metabolic disease. *Cell Metab.* **13**, 11–22 (2011).
13. E. C. Cokorinos, J. Delmore, A. R. Reyes, B. Albuquerque, R. Kjobsted, N. O. Jorgensen, J. L. Tran, A. Jatkar, K. Cialdea, R. M. Esquejo, J. Meissen, M. F. Calabrese, J. Cordes, R. Moccia, D. Tess, C. T. Salatto, T. M. Coskran, A. C. Opsahl, D. Flynn, M. Blatnik, W. Li, E. Kindt, M. Foretz, B. Viollet, J. Ward, R. G. Kurumbail, A. S. Kalgutkar, J. F. P. Wojtaszewski, K. O. Cameron, R. A. Miller, Activation of skeletal muscle AMPK promotes glucose disposal and glucose lowering in non-human primates and mice. *Cell Metab.* **25**, 1147–1159.e10 (2017).
14. T. Jin, The WNT signalling pathway and diabetes mellitus. *Diabetologia* **51**, 1771–1780 (2008).
15. J. H. M. Yung, A. Giacca, Role of c-Jun N-terminal kinase (JNK) in obesity and type 2 diabetes. *Cell* **9**, 706 (2020).
16. J. M. Orozco, P. A. Krawczyk, S. M. Scaria, A. L. Cangelosi, S. H. Chan, T. Kunchok, C. A. Lewis, D. M. Sabatini, Dihydroxyacetone phosphate signals glucose availability to mTORC1. *Nat. Metab.* **2**, 893–901 (2020).
17. C. A. Jaeger-Ruckstuhl, M. Hinterbrandner, S. Hopner, C. E. Correnti, U. Luthi, O. Friedli, S. Freigang, M. F. Al Sayed, E. D. Buhrer, M. A. Amrein, C. M. Schurch, R. Radpour, C. Riether, A. F. Ochsenbein, TNIK signaling imprints $CD8^+$ T cell memory formation early after priming. *Nat. Commun.* **11**, 1632 (2020).
18. C. A. Fu, M. Shen, B. C. Huang, J. Lasaga, D. G. Payan, Y. Luo, TNIK, a novel member of the germinal center kinase family that activates the c-Jun N-terminal kinase pathway and regulates the cytoskeleton. *J. Biol. Chem.* **274**, 30729–30737 (1999).
19. S. H. Raun, C. Henriquez-Olguin, I. Karavaeva, M. Ali, L. L. V. Moller, W. Kot, J. L. Castro-Mejia, D. S. Nielsen, Z. Gerhart-Hines, E. A. Richter, L. Sylow, Housing temperature influences exercise training adaptations in mice. *Nat. Commun.* **11**, 1560 (2020).
20. M. Kleinert, B. L. Parker, T. E. Jensen, S. H. Raun, P. Pham, X. Han, D. E. James, E. A. Richter, L. Sylow, Quantitative proteomic characterization of cellular pathways associated with altered insulin sensitivity in skeletal muscle following high-fat diet feeding and exercise training. *Sci. Rep.* **8**, 10723 (2018).
21. A. K. Picke, L. Sylow, L. L. V. Moller, R. Kjobsted, F. N. Schmidt, M. W. Steejn, J. Salbach-Hirsch, C. Hofbauer, M. Bluher, A. Saalbach, B. Busse, M. Rauner, L. C. Hofbauer, Differential effects of high-fat diet and exercise training on bone and energy metabolism. *Bone* **116**, 120–134 (2018).
22. R. A. DeFronzo, D. Tripathy, Skeletal muscle insulin resistance is the primary defect in type 2 diabetes. *Diabetes Care* **32**Suppl 2, S157–S163 (2009).
23. D. J. Fazakerley, J. R. Krycer, A. L. Kearney, S. L. Hocking, D. E. James, Muscle and adipose tissue insulin resistance: Malady without mechanism? *J. Lipid Res.* **60**, 1720–1732 (2019).
24. J. M. Ng, K. Azuma, C. Kelley, R. Pencek, Z. Radikova, C. Laymon, J. Price, B. H. Goodpaster, D. E. Kelley, PET imaging reveals distinctive roles for different regional adipose tissue depots in systemic glucose metabolism in nonobese humans. *Am. J. Physiol. Endocrinol. Metab.* **303**, E1134–E1141 (2012).
25. B. B. Lowell, B. M. Spiegelman, Towards a molecular understanding of adaptive thermogenesis. *Nature* **404**, 652–660 (2000).
26. C. R. Balistreri, C. Caruso, G. Candore, The role of adipose tissue and adipokines in obesity-related inflammatory diseases. *Mediators Inflamm.* **2010**, 802078 (2010).
27. A. Kharitonenkov, T. L. Shiyanova, A. Koester, A. M. Ford, R. Micanovic, E. J. Galbreath, G. E. Sandusky, L. J. Hammond, J. S. Moyers, R. A. Owens, J. Gromada, J. T. Brozinick, E. D. Hawkins, V. J. Wroblewski, D. S. Li, F. Mehrbod, S. R. Jaskunas, A. B. Shanafelt, FGF-21 as a novel metabolic regulator. *J. Clin. Invest.* **115**, 1627–1635 (2005).
28. J. Xu, D. J. Lloyd, C. Hale, S. Stanislaus, M. Chen, G. Sivits, S. Vonderfecht, R. Hecht, Y. S. Li, R. A. Lindberg, J. L. Chen, D. Y. Jung, Z. Zhang, H. J. Ko, J. K. Kim, M. M. Veniant, Fibroblast growth factor 21 reverses hepatic steatosis, increases energy expenditure, and improves insulin sensitivity in diet-induced obese mice. *Diabetes* **58**, 250–259 (2009).
29. L. D. BonDurant, M. Ameka, M. C. Naber, K. R. Markan, S. O. Idiga, M. R. Acevedo, S. A. Walsh, D. M. Ornitz, M. J. Potthoff, FGF21 regulates metabolism through adipose-dependent and -independent mechanisms. *Cell Metab.* **25**, 935–944.e4 (2017).
30. S. G. Kang, M. J. Choi, S. B. Jung, H. K. Chung, J. Y. Chang, J. T. Kim, Y. E. Kang, J. H. Lee, H. J. Hong, S. M. Jun, H. J. Ro, J. M. Suh, H. Kim, J. Auwerx, H. S. Yi, M. Shong, Differential roles of GDF15 and FGF21 in systemic metabolic adaptation to the mitochondrial integrated stress response. *iScience* **24**, 102181 (2021).
31. A. Vegiopoulos, M. Rohm, S. Herzig, Adipose tissue: Between the extremes. *EMBO J.* **36**, 1999–2017 (2017).
32. M. C. Petersen, G. I. Shulman, Mechanisms of insulin action and insulin resistance. *Physiol. Rev.* **98**, 2133–2223 (2018).
33. Z. Guo, M. D. Jensen, Blood glycerol is an important precursor for intramuscular triacylglycerol synthesis. *J. Biol. Chem.* **274**, 23702–23706 (1999).
34. Y. Macotela, J. Boucher, T. T. Tran, C. R. Kahn, Sex and depot differences in adipocyte insulin sensitivity and glucose metabolism. *Diabetes* **58**, 803–812 (2009).
35. K. L. Grove, S. K. Fried, A. S. Greenberg, X. Q. Xiao, D. J. Clegg, A microarray analysis of sexual dimorphism of adipose tissues in high-fat-diet-induced obese mice. *Int. J. Obes. (Lond)* **34**, 989–1000 (2010).
36. I. Maric, J. P. Krieger, P. van der Velden, S. Borchers, M. Asker, M. Vujicic, I. Wernstedt Asterholm, K. P. Skibicka, Sex and species differences in the development of diet-induced obesity and metabolic disturbances in rodents. *Front. Nutr.* **9**, 828522 (2022).
37. B. C. Martin, J. H. Warram, A. S. Krolewski, R. N. Bergman, J. S. Soeldner, C. R. Kahn, Role of glucose and insulin resistance in development of type 2 diabetes mellitus: Results of a 25-year follow-up study. *Lancet* **340**, 925–929 (1992).
38. Y. J. Kim, H. J. Kim, W. J. Lee, J. K. Seong, A comparison of the metabolic effects of treadmill and wheel running exercise in mouse model. *Lab. Anim. Res.* **36**, 3 (2020).
39. B. F. Vind, C. Pehmoller, J. T. Treebak, J. B. Birk, M. Hey-Mogensen, H. Beck-Nielsen, J. R. Zierath, J. F. Wojtaszewski, K. Højlund, Impaired insulin-induced site-specific phosphorylation of TBC1 domain family, member 4 (TBC1D4) in skeletal muscle of type 2 diabetes patients is restored by endurance exercise-training. *Diabetologia* **54**, 157–167 (2011).
40. J. A. Windelov, J. Pedersen, J. J. Holst, Use of anesthesia dramatically alters the oral glucose tolerance and insulin secretion in C57Bl/6 mice. *Physiol. Rep.* **4**, e12824 (2016).
41. W. Zhang, B. J. Thompson, V. Hietakangas, S. M. Cohen, MAPK/ERK signaling regulates insulin sensitivity to control glucose metabolism in *Drosophila*. *PLOS Genet.* **7**, e1002429 (2011).
42. S. J. Pettitt, Q. Liang, X. Y. Rairdan, J. L. Moran, H. M. Prosser, D. R. Beier, K. C. Lloyd, A. Bradley, W. C. Skarnes, Agouti C57BL/6N embryonic stem cells for mouse genetic resources. *Nat. Methods* **6**, 493–495 (2009).
43. L. L. V. Møller, I. L. Nielsen, J. R. Knudsen, N. R. Andersen, T. E. Jensen, L. Sylow, E. A. Richter, The p21-activated kinase 2 (PAK2), but not PAK1, regulates contraction-stimulated skeletal muscle glucose transport. *Physiol. Rep.* **8**, e14460 (2020).

44. S. H. Raun, M. Ali, R. Kjobsted, L. L. V. Moller, M. A. Federspiel, E. A. Richter, T. E. Jensen, L. Sylow, Rac1 muscle knockout exacerbates the detrimental effect of high-fat diet on insulin-stimulated muscle glucose uptake independently of Akt. *J. Physiol.* **596**, 2283–2299 (2018).
45. P. Ferre, A. Leturque, A. F. Burnol, L. Penicaud, J. Girard, A method to quantify glucose utilization in vivo in skeletal muscle and white adipose tissue of the anaesthetized rat. *Biochem. J.* **228**, 103–110 (1985).
46. P. T. Fueger, D. P. Bracy, C. M. Malabanan, R. R. Pencek, D. H. Wasserman, Distributed control of glucose uptake by working muscles of conscious mice: Roles of transport and phosphorylation. *Am. J. Physiol. Endocrinol. Metab.* **286**, E77–E84 (2004).
47. O. H. Lowry, J. V. Passonneau, *A Flexible System of Enzymatic Analysis* (Academic Press, ed. 3, 1972).
48. A. M. Lundsgaard, J. B. Holm, K. A. Sjoberg, K. N. Bojsen-Moller, L. S. Myrmel, E. Fjaere, B. A. H. Jensen, T. S. Nicolaisen, J. R. Hingst, S. L. Hansen, S. Doll, P. E. Geyer, A. S. Deshmukh, J. J. Holst, L. Madsen, K. Kristiansen, J. F. P. Wojtaszewski, E. A. Richter, B. Kiens, Mechanisms preserving insulin action during high dietary fat intake. *Cell Metab.* **29**, 50–63.e4 (2019).
49. C. Welinder, L. Ekblad, Coomassie staining as loading control in Western blot analysis. *J. Proteome Res.* **10**, 1416–1419 (2011).
50. C. Bycroft, C. Freeman, D. Petkova, G. Band, L. T. Elliott, K. Sharp, A. Motyer, D. Vukcevic, O. Delaneau, J. O'Connell, A. Cortes, S. Welsh, A. Young, M. Effingham, G. McVean, S. Leslie, N. Allen, P. Donnelly, J. Marchini, The UK Biobank resource with deep phenotyping and genomic data. *Nature* **562**, 203–209 (2018).
51. J. D. Szustakowski, S. Balasubramanian, E. Kvikstad, S. Khalid, P. G. Bronson, A. Sasson, E. Wong, D. Liu, J. W. Davis, C. Haefliger, A. K. Loomis, R. Mikkilineni, H. J. Noh, S. Wadhawan, X. Bai, A. Hawes, O. Krasheninina, R. Ulloa, A. E. Lopez, E. N. Smith, J. F. Waring, C. D. Whelan, E. A. Tsai, J. D. Overton, W. J. Salerno, H. Jacob, S. Szalma, H. Runz, G. Hinkle, P. Nioi, S. Petrovski, M. R. Miller, A. Baras, L. J. Mitnaul, J. G. Reid; UKB-ESC Research Team, Advancing human genetics research and drug discovery through exome sequencing of the UK Biobank. *Nat. Genet.* **53**, 942–948 (2021).
52. S. Lee, M. J. Emond, M. J. Bamshad, K. C. Barnes, M. J. Rieder, D. A. Nickerson; NHLBI GO Exome Sequencing Project—ESP Lung Project Team, D. C. Christiani, M. M. Wurfel, X. Lin, Optimal unified approach for rare-variant association testing with application to small-sample case-control whole-exome sequencing studies. *Am. J. Hum. Genet.* **91**, 224–237 (2012).

Acknowledgments: We acknowledge the skilled technical assistance of B. Bolmgren and I. Bech Nielsen (Department of Nutrition, Exercise and Sports, Faculty of Science, University of Copenhagen, Denmark), A. Jokipii-Utzon (Institute of Sports Medicine, Bispebjerg Hospital, Denmark), and A. Sharma Friismose (Department of Cellular and Molecular Medicine, Morphogenesis and Differentiation Program, Panum Institute, University of Copenhagen, Denmark). The FIMM metabolomics unit was supported by HiLIFE and Biocenter Finland. We are grateful to A. Klip (SickKids Research Institute, The Hospital for Sick Children, Toronto, ON, Canada) for gifting the C2C12 WT cell line. **Funding:** The study was supported by grants from Novo Nordisk Foundation NNF18OC0032082 (to L.S.), Novo Nordisk Foundation NNF16OC0023418 (to L.S.), Novo Nordisk Foundation NNF20OC0063577 (to L.S.), Independent Research Fund Denmark 9039-00170B (to L.S.), Independent Research Fund Denmark 0169-00013B (to L.S.), the European Union's Horizon 2020 research and innovation programme, Marie Skłodowska-Curie grant agreement no. 801199 (to T.C.P.P. and E.A.R.), Finnish Diabetes Research Foundation (to E.H.), Orion Research Foundation (to E.H.), Maud Kuistila Foundation (to E.H.), German Research Foundation, Collaborative Research Center SFB 684 (to A.K.), Lundbeck Foundation R322-2019-2688 (to L.L.V.M.), Independent Research Fund Denmark 2030-00007A (to S.H.R.), Lundbeck Foundation R380-2021-1451 (to S.H.R.), Academy of Finland (to A.S.), Sigrid Jusélius Foundation (to A.S.), Jane and Aatos Erkko Foundation (to A.S.), and the Hallas-Møller Emerging Investigator Novo Nordisk Foundation NNF17OC0031204 (to M.S.O.).
Author contributions: Conceptualization: T.C.P.P., E.H., and L.S. Methodology: T.C.P.P., L.D., A.J., A.K., M.S.O., P.S., A.I.N., and E.H. Investigation: T.C.P.P., L.D., M.S.A., S.H.R., L.L.V.M., A.J., N.D., N.R.A., A.M.F., Z.G.-H., B.K., A.S., S.J.S., A.K., M.S.O., P.S., A.I.N., E.A.R., E.H., and L.S. Visualization: T.C.P.P. Supervision: E.A.R. and L.S. Writing (original draft): T.C.P.P., E.H., and L.S. Writing (review and editing): L.D., M.S.A., S.H.R., L.L.V.M., A.J., N.R.A., A.M.F., Z.G.-H., B.K., A.S., S.J.S., A.K., M.S.O., P.S., A.I.N., and E.A.R. **Competing interests:** The authors declare that they have no competing interests. **Data and materials availability:** All data needed to evaluate the conclusions in the paper are present in the paper and/or the Supplementary Materials.

Submitted 9 November 2022
Accepted 7 July 2023
Published 9 August 2023
10.1126/sciadv.adf7119